

1 **Holocene climates of the Iberian Peninsula: pollen-based reconstructions of changes in**  
2 **the west-east gradient of temperature and moisture**

3 Mengmeng Liu<sup>1\*</sup>, Yicheng Shen<sup>2</sup>, Penelope González-Sampériz<sup>3</sup>, Graciela Gil-Romera<sup>3</sup>,  
4 Cajo J. F. ter Braak<sup>4</sup>, Iain Colin Prentice<sup>1</sup>, Sandy P. Harrison<sup>2</sup>

5 1: Department of Life Sciences, Imperial College London, Silwood Park Campus, Buckhurst  
6 Road, Ascot SL5 7PY, UK

7 2: Geography & Environmental Science, Reading University, Whiteknights, Reading, RG6  
8 6AH, UK

9 3: Instituto Pirenaico de Ecología-CSIC, Avda. Montaña 1005, 50059, Zaragoza, Spain

10 4: Biometris (Applied Mathematics and Applied Statistics Centre), Wageningen University &  
11 Research, 6708 PB Wageningen, The Netherlands

12 \*: Corresponding author: Mengmeng Liu (m.liu18@imperial.ac.uk)

13 Ms for: *Climate of the Past*

14 **Abstract**

15 The Iberian Peninsula is characterised by a steep west-east moisture gradient today, reflecting  
16 the dominance of maritime influences along the Atlantic coast and more Mediterranean-type  
17 climate further east. Holocene pollen records from the Peninsula suggest that this gradient was  
18 less steep during the mid-Holocene, possibly reflecting the impact of orbital changes on  
19 circulation and thus regional patterns in climate. Here we use 7214 pollen samples from 117  
20 sites covering part or all of the last 12,000 years to reconstruct changes in seasonal temperature  
21 and in moisture across the Iberian Peninsula quantitatively. We show that there is an increasing  
22 trend in winter temperature at a regional scale, consistent with known changes in winter  
23 insolation. However, summer temperatures do not show the decreasing trend through the  
24 Holocene that would be expected if they were a direct response to insolation forcing. We show  
25 that summer temperature is strongly correlated with plant-available moisture ( $\alpha$ ), as measured  
26 by the ratio of actual evapotranspiration to equilibrium evapotranspiration, which declines  
27 through the Holocene. The reconstructions also confirm that the west-east gradient in moisture  
28 was considerably less steep than today during the mid-Holocene, indicating that atmospheric  
29 circulation changes (possibly driven by orbital changes) have been important determinants of  
30 the Holocene climate of the region.

31 **1. Introduction**

32 The Iberian Peninsula is characterised by a steep west-east gradient in temperature and  
33 moisture today, reflecting the dominance of maritime influences along the Atlantic coast and  
34 more Mediterranean-type climate further east. Projections of future climate change suggest that  
35 the region will become both warmer and drier, but nevertheless show that this west-east  
36 differentiation is maintained (Andrade et al., 2021a). The changes in temperature are projected  
37 to be larger and the occurrence of extreme temperature episodes more frequent in the south-  
38 central and eastern parts of Iberia than in Atlantic coastal areas (Carvalho et al., 2021). Similar  
39 gradients are seen in future projections of precipitation change, with largest reductions in  
40 precipitation in the south-central region (Andrade et al., 2021b). However, the stability of these  
41 west-east gradients during the Holocene has been questioned. In particular, the west-east  
42 gradient in moisture appears to have been less pronounced during the mid-Holocene (8~4 ka)  
43 when cooler summers and wetter conditions in the Atlantic zone (e.g. Martínez-Cortizas et al.,  
44 2009; Mauri et al., 2015) coincided with the maximum development of mesophytic vegetation  
45 further east and south (Aranbarri et al., 2014, 2015; Carrión et al., 2010, 2009; González-  
46 Sampériz et al., 2017).

47 However, much of the evidence for Holocene climates of the Iberian Peninsula is based on  
48 qualitative interpretations of vegetation changes, generally interpreted as reflecting changes in  
49 moisture availability (Morellón et al., 2018; Ramos-Román et al., 2018; Schröder et al., 2019).  
50 These records are extensive and they seem to indicate fairly complex spatial patterns of change.  
51 Kaufman et al. (2020) provides quantitative reconstructions of summer and winter temperature  
52 in their compilation of Holocene climate information, but there are only 5 terrestrial sites from  
53 the Iberian Peninsula. Iberia was also included in the quantitative pollen-based reconstructions  
54 of European climate through the Holocene in Mauri et al. (2015), which is an update of Davis  
55 et al. (2003). However, the geographical distribution of sites included is uneven and a large  
56 fraction of the records were from the Pyrenees and the Cantabrian mountains, with additional  
57 clustering of sites in coastal regions. Thus, the inferred patterns of climate over most of the  
58 central part of the Peninsula are therefore largely extrapolated. Tarroso et al. (2016) has  
59 provided reconstructions of summer and winter temperature and mean annual precipitation  
60 since the Last Glacial Maximum for the Iberian Peninsula, by using modern species distribution  
61 data to develop climate probability distribution functions (PDFs) and applying these to 31 fossil  
62 records. However, although they identified trends in precipitation during the Holocene, the

63 temperature reconstructions do not seem to be reliable since they show no changes through  
64 time (9~3 ka), either for the Iberian Peninsula as a whole or for individual sub-regions, in  
65 contradiction to the other reconstructions. The current state of uncertainty about Holocene  
66 climate changes in Iberia is further exacerbated because quantitative reconstructions of summer  
67 temperature made at individual sites using chironomid data (Muñoz Sobrino et al., 2013;  
68 Tarrats et al., 2018) are not consistent with reconstructed summer temperatures based on pollen  
69 for the same sites.

70 We used the method Tolerance-weighted Weighted Average Partial Least-Squares regression  
71 with a sampling frequency correction (fxTWA-PLS), introduced by Liu et al. (2020) as an  
72 improvement of the widely used Weighted Average Partial Least-Squares (WAPLS: ter Braak  
73 and Juggins, 1993) method for reconstructing past climates from pollen assemblages. As  
74 presented in depth by Liu et al. (2020), this method is a more complete implementation of the  
75 theory underlying WA-PLS because it takes greater account of the climatic information  
76 provided by taxa with more limited climatic ranges and also applies the sampling frequency  
77 correction to reduce the impact of uneven sampling in the training data set. Liu et al. (2020)  
78 showed that fxTWA-PLS does indeed provide better reconstructions than WA-PLS.

79 Here we have further modified the algorithm implementing fxTWA-PLS, achieving an  
80 additional gain in performance. In the algorithm as published by Liu et al. (2020), sampling  
81 frequencies were extracted from a histogram. In the modified algorithm they are estimated  
82 using P-splines smoothing (Eilers and Marx, 2021), which makes the estimates almost  
83 independent on the chosen bin width (see Appendix A for details). In addition, the modified  
84 method applies the sampling frequency correction at two separate steps – the estimation of  
85 optima and tolerances, and the regression step – a measure intended to produce more stable  
86 results. Indeed, the modified method produces both improved  $R^2$  values and reduced  
87 compression and maximum bias in reconstructed climate variables (see Table A1 and Figs A1–  
88 A2). We will return to this point in the Discussion.

89 We have used this improved method to reconstruct Holocene climates across Iberia, and re-  
90 examined the trends in summer and winter temperature and plant-available moisture, using a  
91 new and relatively comprehensive compilation of pollen data (Shen et al., 2022) with age  
92 models based on the latest radiocarbon calibration curve (IntCal20: Reimer et al., 2020). We  
93 explicitly test whether there are significant differences in the west-east gradient of moisture  
94 and temperature through time. We then analyse the relationships between the changes in the

95 three climate variables and how trends in these variables are related to external climate forcing.  
96 These analyses allow us to investigate whether the west-east gradient in moisture was less steep  
97 during the mid-Holocene and explore what controls the patterns of climate change across the  
98 region.

99 **2. Methods**

100 Multiple techniques have been developed to make quantitative climate reconstructions from  
101 pollen (see reviews in Bartlein et al., 2011; Chevalier et al., 2020; Salonen et al., 2011). Modern  
102 analogue techniques (MAT: Overpeck et al., 1985) tend to produce rapid shifts in reconstructed  
103 values corresponding to changes in the selection of the specific analogue samples, although  
104 this tendency is less marked in the conceptually analogous response surface technique (Bartlein  
105 et al., 1986). Regression-based techniques, including weighted averaging methods such as  
106 Weighted Average Partial Least-Squares (WAPLS: ter Braak and Juggins, 1993), do not  
107 produce step-changes in the reconstructions but suffer from the tendency to compress the  
108 reconstructions towards the central part of the sampled climate range. However, this tendency  
109 can be substantially reduced by accounting for the sampling frequency ( $f_x$ ) and the climate  
110 tolerance of the pollen taxa present in the training data set ( $f_x$ TWA-PLS: Liu et al., 2020).  
111 Machine-learning and Bayesian approaches have also been applied to derive climate  
112 reconstructions from pollen assemblages (Peyron et al., 1998; Salonen et al., 2019). However,  
113 comparison of  $f_x$ TWA-PLS with the Bayesian model BUMPER (Holden et al., 2017), shows  
114 that  $f_x$ TWA-PLS performs better in capturing the climate of the modern training data set from  
115 Europe (Liu et al., 2020).

116 Although  $f_x$ TWA-PLS has clear advantages over other quantitative reconstructions techniques,  
117 there is still a slight tendency towards compression. We have therefore made a further  
118 modification to the approach as described in Liu et al. (2020). In the original version of  
119  $f_x$ TWA-PLS, the  $f_x$  correction is applied as a weight with the form of  $1/f_x^2$  in the regression  
120 (step 7 in Table 1 in Liu et al., 2020). Here (see Appendix A) we make a further modification  
121 of  $f_x$ TWA-PLS by (a) applying the  $f_x$  correction separately in both the taxon calculation and  
122 the regression (step 2 and 7 in Table 1 in Liu et al., 2020) as a weight with the form of  $1/f_x$  and  
123 (b) applying P-splines smoothing (Eilers and Marx, 2021) in order to reduce the dependence  
124 of the  $f_x$  estimation on bin width. The modified version further reduces the biases at the  
125 extremes of the sampled climate range.

126 There are no generally accepted rules as to the choice of variables for palaeoclimate  
127 reconstruction. No systematic comparison of these choices has been made. However, it is  
128 widely understood that plant taxon distributions reflect distinct, largely independent controls  
129 by summer temperatures, winter temperatures, and moisture availability (see e.g. Harrison et  
130 al., 2010). Therefore, in common with many other studies (Cheddadi et al., 1997; Jiang et al.,  
131 2010; Peyron et al., 1998; Wei et al., 2021; Zhang et al., 2007), we have chosen bioclimatic  
132 variables that reflect these independent controls, with mean temperature of the coldest month  
133 (MTCO) to represent winter temperatures, mean temperature of the warmest month (MTWA)  
134 to represent summer temperatures and  $\alpha$ , an estimate of the ratio of actual evapotranspiration  
135 to equilibrium evapotranspiration, to represent plant-available moisture. We choose not to use  
136 mean annual air temperature (MAAT) because it is a composite of summer and winter  
137 conditions; and we prefer to use an index of effective moisture availability (our estimate of  $\alpha$   
138 being one such index) to mean annual precipitation (MAP), whose significance for plant  
139 function depends strongly on potential evaporation (a function of temperature and net  
140 radiation). Our calculation of  $\alpha$  takes account of this dependence. Growing degree days above  
141 a baseline of 0 °C (GDD<sub>0</sub>) would be a possible alternative to MTWA as an expression of  
142 summer conditions but is most relevant as a predictor of “cold limits” of trees in cool climates,  
143 whereas MTWA better reflects the high-temperature stress on plants in Mediterranean-type  
144 climates.

145 We used the modified version of fxTWA-PLS to reconstruct these three climate variables. The  
146 individual and joint effects of MTCO, MTWA and  $\alpha$  were tested explicitly using canonical  
147 correspondence analysis (CCA). The modified version further reduces the biases at the  
148 extremes of the sampled climate range, while retaining the desirable properties of WA-PLS in  
149 terms of robustness to spatial autocorrelation (fxTWA-PLS: Liu et al., 2020).

150 The modern pollen training dataset was derived from the SPECIAL Modern Pollen Data Set  
151 (SMPDS: Harrison, 2019). The SMPDS consists of relative abundance records from 6458  
152 terrestrial sites from Europe, northern Africa, the Middle East and northern Eurasia (SI Fig.  
153 S1) assembled from multiple different published sources. The pollen records were  
154 taxonomically standardized, and filtered (as recommended by Chevalier et al., 2020) to remove  
155 obligate aquatics, insectivorous species, introduced species, and taxa that only occur in  
156 cultivation (see SI Table S1 for the list). Taxa (mainly herbaceous) with only sporadic  
157 occurrences were amalgamated to higher taxonomic levels (genus, sub-family or family) after

158 ensuring consistency with their distribution in climate space. As a result of these  
159 amalgamations, the SMPDS contains data on 247 pollen taxa. For our analysis, we use the 195  
160 taxa that occur at more than 10 sites.

161 Modern climate data at each of the sites in the training data set were obtained from Harrison  
162 (2019). This data set contains climate reconstructions of MTCO, growing degree days above a  
163 baseline of 0° C (GDD<sub>0</sub>) and a moisture index (MI), defined as the ratio of annual precipitation  
164 to annual potential evapotranspiration. The climate at each site was obtained using  
165 geographically weighted regression (GWR) of the CRU CL v2.0 gridded dataset of modern  
166 (1961-1990) surface climate at 10 arc minute resolution (New et al., 2002) in order to (a)  
167 correct for elevation differences between each pollen site and the corresponding grid cell and  
168 (b) make the resulting climate independent of the resolution of the underlying data set. The  
169 geographically weighted regression used a fixed bandwidth kernel of 1.06 ° (~140km) to  
170 optimize model diagnostics and reduce spatial clustering of residuals relative to other  
171 bandwidths. The climate of each pollen site was then estimated based on its longitude, latitude,  
172 and elevation. MTCO and GDD<sub>0</sub> was taken directly from the GWR regression and MI was  
173 calculated for each pollen site using a modified code from SPLASH v1.0 (Davis et al., 2017)  
174 based on daily values of precipitation, temperature and sunshine hours again obtained using a  
175 mean-conserving interpolation of the monthly values of each. For this application, we used  
176 MTCO directly from the data set but calculated MTWA from MTCO and GDD<sub>0</sub>, based on the  
177 relationship between MTCO, MTWA and GDD<sub>0</sub> given by Appendix 2 of Wei et al. (2021).  
178 We derived  $\alpha$  from MI following Liu et al. (2020). The modern training data set provides  
179 records spanning a range of MTCO from – 42.4 °C to 14.8 °C, of MTWA from 4.2 °C to 33.5  
180 °C, and of  $\alpha$  from 0.04 to 1.25 (Fig. 1, SI Fig. S1).

181 The fossil pollen data from the Iberian Peninsula were compiled by Shen et al. (2021) and the  
182 data set was obtained from Harrison et al. (2022). The taxonomy used by Shen et al. (2021) is  
183 consistent with that employed in the SMPDS. Shen et al. (2021) provides consistent age models  
184 for all the records based on the IntCal20 calibration curve (Reimer et al., 2020) and the BACON  
185 Bayesian age-modelling tool (Blaauw et al., 2021; Blaauw and Christeny, 2011) using the  
186 supervised modelling approach implemented in the `ageR` package (Villegas-Diaz et al, 2021).  
187 We excluded individual pollen samples with large uncertainties (standard error larger than 100  
188 years) on the attributed in the new age model. As a result, the climate reconstructions are based  
189 on a fossil data set of 7384 pollen samples from 117 records covering part or all of the last

190 12,000 years (Fig. 2), with 42 individual records provided by the original authors, 73 records  
191 obtained from the European Pollen Database (EPD, [www.europeanpollendatabase.net](http://www.europeanpollendatabase.net)) and 2  
192 records from PANGAEA ([www.pangaea.de/](http://www.pangaea.de/)). Details of the records are given in Table 1. The  
193 average temporal resolution of these records is 101 years. We then excluded a few samples  
194 where the reconstructed values of  $\alpha$  exceed the natural limit of 0 and 1.26. Finally, 7214  
195 samples from 117 records are used for the analyses of the climate reconstructions. Summer  
196 insolation and winter insolation are also calculated using the PAST software based on the age  
197 and latitude of each sample (Hammer et al., 2001).

198 Variance inflation factor (VIF) scores are calculated for both the modern climates and the  
199 climates reconstructed from fossil pollen records, in order to avoid multicollinearity problems  
200 and thus guarantee the climate variables (MTCO, MTWA,  $\alpha$ ) used here represent independent  
201 features of the pollen records.

202 In addition to examining the reconstructions for individual sites, we constructed composite  
203 curves for the Iberian Peninsula as a whole. The composite curves provide a way of comparing  
204 the relationship between trends in the reconstructed climate changes and insolation changes.  
205 The curves were constructed after binning the site-based reconstructions using  $\pm 500$ -year bins.  
206 We did 1000 bootstrap resampling of the reconstructed climate values in each  $\pm 500$ -year bin  
207 to avoid the influence of a single value or a single site on the mean climate value in this bin,  
208 and use the standard deviation of the 1000 values to represent the uncertainty of the mean  
209 climate value. We constructed linear regression plots to examine the longitudinal and  
210 elevational patterns in the reconstructed climate variables, and assessed the significance of  
211 differences in these trends through time compared to the most recent bin (0.5 ka  $\pm 500$  years)  
212 based on  $p$  values, with the customary threshold of 0.05. We then compared the climate trends  
213 with changes in summer and winter insolation.

### 214 3. Results

215 The modified version of fxTWA-PLS reproduces the modern climate reasonably well (Table  
216 2). The performance is best for MTCO ( $R^2$  0.75, RMSEP 4.70, slope 0.91) but is also good for  
217  $\alpha$  ( $R^2$  0.68, RMSEP 0.16, slope 0.78) and MTWA ( $R^2$  0.57, RMSEP 3.47, slope 0.71). The  
218 correlations between pollen records and each of the three bioclimate variables, as assessed by  
219 CCA, were strong for both modern climate data and fossil reconstructions (Table 3). The  
220 variance inflation factor (VIF) scores are all less than 6, so there are no multicollinearity

221 problems (Table 3) (Allison, 1994), making it possible to independently reconstruct all three  
222 climate variables based on pollen data. Furthermore, the taxa that contribute most strongly to  
223 reconstructing colder/warmer or wetter/drier climates show predictable patterns consistent with  
224 their known ecological preferences (SI Table S2).

225 Winters were generally colder than present during the early to mid-Holocene, as shown by the  
226 coherent patterns of reconstructed anomalies at individual sites (Fig. 3a, 3d). Here “present”  
227 means the most recent pollen bin ( $0.5 \text{ ka} \pm 500 \text{ years}$ ). The composite curve also shows a  
228 general increase in winter temperatures through time (Fig. 4a), consistent with the trend in  
229 winter insolation (Fig. 4d). The composite curve shows that it was ca  $4^\circ\text{C}$  cooler than today at  
230  $11.5 \text{ ka}$  and conditions remained cooler than present until ca  $2.5 \text{ ka}$ . Winter temperatures today  
231 increase from north to south and are also affected by elevation; these patterns are still present  
232 in the Holocene reconstructions, but there is no spatial differentiation between western and  
233 eastern Iberia in the anomalies (Table 4, SI Fig. S2). The similarity of the changes compared  
234 to present geographically is consistent with the idea that the changes in winter temperature are  
235 driven by changes in winter insolation.

236 Summers were somewhat hotter than present in the west and cooler than present in the east  
237 during the early and mid-Holocene, as shown by the reconstructed anomalies at individual sites  
238 (Fig. 3b, 3e). This west-east difference could not arise if the changes in summer temperatures  
239 were a direct reflection of the insolation forcing (Fig. 4e). Indeed, the composite curve shows  
240 relatively little change in MTWA (Fig. 4b), confirming that there is no direct relationship to  
241 insolation forcing (Fig. 4e).

242 There is a strong west-east gradient in  $\alpha$  at the present day (Fig. 2), with wetter conditions in  
243 the west and drier conditions in the east. However, the reconstructed anomalies at individual  
244 sites (Fig. 3c, 3f) suggest that west was drier and the east was wetter than present in the mid-  
245 Holocene, resulting in a flatter west-east gradient. The west-east gradient is significantly  
246 different from present between  $9.5 \sim 3.5 \text{ ka}$  (Fig. 5, Table 4), implying stronger moisture  
247 advection into the continental interior during the mid-Holocene. The change in gradient is seen  
248 in both high and low elevation sites (SI Fig. S3). There is also significant change in  $\alpha$  with  
249 elevation between  $9.5 \sim 4.5 \text{ ka}$  (Table 4, SI Fig. S4).

250 Summer temperatures are strongly correlated with changes in  $\alpha$ , both in terms of spatial  
251 correlations in the modern data set at a European scale and in terms of spatial and temporal

correlations the fossil data set from Iberian Peninsula (Fig. 6). The patterns of reconstructed anomalies in MTWA and  $\alpha$  at individual sites are also coherent (Fig. 3b, 3c, 3e, 3f), showing drier conditions and hotter summers than present in the west and wetter conditions with cooler summers in the east during the early to mid-Holocene. The west-east gradient in MTWA was significantly different from present between 9.5 and 3.5 ka except 8.5 ka (Table 4, SI Fig. S5), roughly the interval when the gradient in  $\alpha$  was also significantly different from present. Again, the change in the east-west gradient is registered at both high and low elevation sites (SI Fig. S6). However, there is no significant change in MTWA with elevation except 8.5 and 7.5 ka (Table 4, SI Fig. S7).

#### 4. Discussion

The modified version of fxTWA-PLS (fxTWA-PLS2) (Table 2, Table A1) shows a few differences compared to the previous version (fxTWA-PLS1). Cross-validation  $R^2$  values are higher for MTCO and MTWA, and almost unchanged for  $\alpha$ . The maximum bias shows a decrease for all the three variables, especially for MTCO. The compression problem is also reduced for MTCO ( $b_1$  increases from 0.82 to 0.91) and MTWA ( $b_1$  increases from 0.69 to 0.71) while remaining roughly the same for  $\alpha$ . The overall performance statistics thus show substantial improvements for MTCO and MTWA, while they show little change for  $\alpha$ . However, Figure A1 shows that “unphysical” reconstructions beyond the natural limits of  $\alpha$  (0–1.26) are greatly reduced, especially for the lower limit. There are also fewer outliers in Figure A1 and A2 for all three variables. Thus overall, the modified version further reduces the reconstruction biases, especially at the extremes of the sampled climate range. This improvement probably occurs because of the separate application of 1/fx correction during both the calculation of optima and tolerances of taxa and during the regression step – instead of applying an overall weight of 1/fx<sup>2</sup> at the regression step, which can result in some extreme values (with low sampling frequency) being weighed too strongly and appearing as outliers.

fxTWA-PLS2 reconstructed climates have shown that there was a gradual increase in MTCO over the Holocene, both for most of the individual sites represented in the data set (Fig. 3) and for Iberia as a whole (Fig. 4). Colder winters in southern Europe during the mid-Holocene (6 ka) are a feature of many earlier reconstructions (e.g. Cheddadi et al., 1997; Wu et al., 2007). A general warming trend over the Holocene is seen in gridded reconstructions of winter season (December, January, February) temperatures as reconstructed using the modern analogue approach by Mauri et al. (2015), although there is somewhat less millennial-scale variability

284 in these reconstructions (Fig. 7). Nevertheless, their reconstructions show a cooling of 3°C in  
285 the early Holocene, comparable in magnitude to the ca 4°C cooling at 11.5 ka reconstructed  
286 here. Although they show conditions slightly cooler than present persisting up to 1 ka, the  
287 differences are very small (ca 0.5°C) after 2 ka, again consistent with our reconstructions of  
288 MTCO similar to present by 2.5 ka. Quantitative reconstructions of winter temperature for the  
289 5 terrestrial sites from the Iberian Peninsula in the Kaufman et al. (2020) compilation all show  
290 a general trend of winter warming over the Holocene, but the magnitude of the change at some  
291 of the individual sites is much larger (ca 10°C) and there is no assessment of the uncertainty  
292 on these reconstructions. The composite curve of Kaufman et al. (2020) shows an increasing  
293 trend in MTCO through the Holocene although with large uncertainties (Fig. 7). In contrast to  
294 the consistency of the increasing trend in MTCO during the Holocene between our  
295 reconstructions and those of Mauri et al. (2015) and Kaufman et al. (2020), there is no  
296 discernible trend in MTCO during the Holocene reconstruction of Tarroso et al. (2016). Indeed,  
297 there is no significant change in their MTCO values after ca 9 ka, either for the Peninsula as a  
298 whole (Fig. 7) or for any of the four sub-regions they considered. Our reconstructed trend in  
299 winter temperature is consistent with the changes in insolation forcing at this latitude during  
300 the Holocene, and is also consistent with transient climate model simulations (Braconnot et al.,  
301 2019; Carré et al., 2021; Dallmeyer et al., 2020; Parker et al., 2021) of the winter temperature  
302 response to changing insolation forcing over the late Holocene in this region (Fig. 8, SI Fig.  
303 S8). Thus, we suggest that changes in winter temperatures are a direct consequence of  
304 insolation forcing.

305 We have shown that there is no overall trend in MTWA during the Holocene (Fig. 4).  
306 According to our reconstructions, summer temperatures fluctuated between ca 0.5°C above or  
307 below modern temperature. The lack of coherent trend in MTWA is consistent with the gridded  
308 reconstructions of summer (June, July, August) temperature in the Mauri et al. (2015) data set  
309 and also with the 5 terrestrial sites from Iberia included in the Kaufman et al. (2020) data set.  
310 However, the patterns shown in the three data sets are very different from one another. Mauri  
311 et al. (2015) suggest the early Holocene was colder than today, and although temperatures  
312 similar to today were reached at 9 ka, most of the Holocene was characterised by cooler  
313 summers. Kaufman et al. (2020), however, showed warmer than present conditions during the  
314 early Holocene although they also show cooler conditions during the later Holocene. The  
315 differences between the three data sets could reflect differences in the reconstruction methods,  
316 or differences in the number of records used and in the geographic sampling. However, given

317 the fact that all three data sets show similar trends in winter temperature, the lack of coherency  
318 between the data sets for MTWA points to there not being a strong, regionally coherent signal  
319 of summer temperature changes during the Holocene. Tarroso et al. (2016) also showed no  
320 significant changes in MTWA after ca 9 ka (Fig. 7).

321 The chironomid record from Laguna de la Roya covers the late glacial and terminates at 10.5  
322 ka (Muñoz Sobrino et al., 2013). The reconstructed July temperature during the early Holocene  
323 is ca 12~13 °C, which is considerably cooler than today at this site. However, the authors  
324 caution that these samples have poor analogues and the record should be interpreted with  
325 caution. Chironomid-based reconstructions of July temperature at Basa de la Mora (Tarrats et  
326 al., 2018), a high elevation site in the Pyrenees, indicate temperatures within  $\pm 0.5^\circ$  C of the  
327 modern during the early to mid-Holocene (10~6 ka), similar to our regional composite  
328 reconstructions. However, they show persistently conditions cooler than present by ca 1.5 °C  
329 between 4.5 and 2 ka, not seen in our reconstructions. Furthermore, direct comparison of our  
330 reconstructions of MTWA at Basa de la Mora (SI Fig. S9) to the chironomid-based  
331 reconstructions highlights that the two records show very different trajectories, since the  
332 pollen-based reconstruction of this site shows a consistent warming trend throughout the  
333 Holocene. Although Tarrats et al. (2018) argue that discrepancies between their temperature  
334 reconstructions and pollen-based reconstructions reflects the fact that the vegetation of Iberia,  
335 including the mountain areas, is largely driven by moisture changes and perhaps is not a good  
336 indicator of temperature, we have shown that there is sufficient information in the pollen  
337 records to reconstruct temperature and moisture independently (Table 3, Table S2). Thus, the  
338 cause of the differences between the pollen-based and chironomid-based reconstructions at  
339 Basa de la Mora is presumably related to methodology. In particular, the chironomid  
340 reconstructions use a training data set that does not include samples from the Pyrenees, or  
341 indeed the Mediterranean more generally, and may therefore not provide good analogues for  
342 Holocene changes at this site.

343 The lack of a clear trend in MTWA in our reconstructions (Fig. 4b) is not consistent with  
344 insolation forcing (Fig. 4e), which shows a declining trend during the Holocene nor is it  
345 consistent with simulated changes in MTWA in transient climate model simulations of the  
346 summer temperature response to changing insolation forcing over the Holocene in this region  
347 (Fig. 8). The change in moisture gradient during the mid-Holocene, however, suggests an  
348 alternative explanation whereby changes in summer temperature are a response to land-surface

349 feedbacks associated with changes in moisture (Fig. 6). Specifically, the observed increased  
350 advection of moisture into eastern Iberia would have created wetter conditions there, which in  
351 turn would permit increased evapotranspiration, implying less allocation of available net  
352 radiation to sensible heating, and resulting in cooler air temperatures. Our reconstructions show  
353 that the west-east moisture gradient in mid-Holocene (Fig. 5) was significantly flatter than the  
354 steep moisture gradient today (Fig. 2), implying a significant increase in moisture advection  
355 into the continental interior during this period. Mauri et al. (2015) also showed that summers  
356 were generally wetter than present in the east but drier than present in the west at early to mid-  
357 Holocene, supporting the idea of a flatter west-east gradient.

358 We have shown that stronger moisture advection is not a feature of transient climate model  
359 simulations of the Holocene, which may explain why these simulations do not show a strong  
360 modification of the insolation-driven changes in summer temperature (Fig. 8). Although the  
361 amplitude differs, all of the models show a general decline in summer temperature. The failure  
362 of the current generation of climate models to simulate the observed strengthening of moisture  
363 transport into Europe and Eurasia during the mid-Holocene has been noted for previous  
364 versions of these models (e.g. Bartlein et al., 2017; Mauri et al., 2014) and also shown in Fig.  
365 S8. Mauri et al. (2014), for example, showed that climate models participating in the last phase  
366 of the Coupled Model Intercomparison Project (CMIP5/PMIP3) were unable to reproduce  
367 reconstructed climate patterns over Europe at 6000 yr B.P. and indicated that this resulted from  
368 over-sensitivity to changes in insolation forcing and the failure to simulate increased moisture  
369 transport into the continent. Bartlein et al. (2017) showed that the CMIP5/PMIP3 models  
370 simulated warmer and drier conditions in mid-continental Eurasia at 6000 yr B.P., inconsistent  
371 with palaeo-environmental reconstructions from the region, as a result of the simulated  
372 reduction in the zonal temperature gradient which resulted in weaker westerly flow and reduced  
373 moisture fluxes into the mid-continent. They also pointed out the strong feedback between drier  
374 conditions and summer temperatures. The drying of the mid-continent is also a strong feature  
375 of the mid-Holocene simulations made with the current generation of CMIP6/PMIP4 models  
376 (Brierley et al., 2020). The persistence of these data-model mismatches highlights the need for  
377 better modelling of land-surface feedbacks on atmospheric circulation and moisture.

378 There are comparatively few pollen-based reconstructions of moisture changes during the  
379 Holocene from Iberia. Records from Padul show increased mean annual and winter  
380 precipitation during the early and mid-Holocene (Camuera et al., 2022; García-Alix et al.,

381 2021). Reconstructions of mean annual and winter precipitation (Camuera et al., 2022) and the  
382 ratio of annual precipitation to annual potential evapotranspiration (Wei et al., 2021) also show  
383 wetter conditions at this time at El Cañizar de Villarquemado. Both of these sites lie in the  
384 eastern part of the Iberian Peninsula, so these reconstructions are consistent with our  
385 interpretation of wetter conditions in this region during the interval between 9.5 and 3.5 ka.  
386 Ilvonen et al. (2022) provide pollen-based reconstructions of mean annual, summer and winter  
387 precipitation from 8 sites in Iberia, using WAPLS and a Bayesian modelling approach.  
388 Although they focus on the contrasting pattern of hydroclimate evolution between northern and  
389 southern Iberia, the three easternmost sites (San Rafael, Navarres, and Qintanar de la Sierra)  
390 show much wetter conditions during the early to mid-Holocene. With the exception of the  
391 record from Monte Areo, the records from further west are relatively complacent and indeed  
392 two sites (Zalamar, El Maillo) show decreased precipitation between 8 and 4 ka. Thus, these  
393 records are consistent with our interpretation that the west-east gradient of moisture was  
394 reduced between 9.5 and 4.5 ka.

395 Speleothem oxygen-isotope data from the Iberian Peninsula provide support for our pollen-  
396 based reconstructions of changes in the west-east gradient of moisture through the Holocene.  
397 The speleothem records show a progressive increase in temperature from the Younger Dryas  
398 onwards, although the trend is less marked in the west than the east (Baldini et al., 2019). This  
399 warming trend is consistent with our reconstructions of changes in MTCO through the  
400 Holocene. Speleothem records also show distinctly different patterns in moisture availability,  
401 with sites in western Iberia indicating wetter environments during early Holocene and a  
402 transition to drier conditions from ca 7.5 cal ka BP to the present (Stoll et al., 2013; Thatcher  
403 et al., 2020) while eastern sites record wetter conditions persisting from 9 to 4 cal ka (Walczak  
404 et al., 2015). This finding would support the weaker west to east moisture gradient shown by  
405 our results.

406 Pollen data are widely used for the quantitative reconstruction of past climates (see discussion  
407 in Bartlein et al., 2011), but reconstructions of moisture indices are also affected by changes in  
408 water-use efficiency caused by the impact of changing atmospheric CO<sub>2</sub> levels on plant  
409 physiology (Farquhar, 1997; Gerhart and Ward, 2010; Prentice et al., 2017; Prentice and  
410 Harrison, 2009). This has been shown to be important on glacial-interglacial timescales, when  
411 intervals of lower-than-present CO<sub>2</sub> result in vegetation appearing to reflect drier conditions  
412 than were experienced in reality (Prentice et al., 2011, 2017; Wei et al., 2021). We do not

413 account for this CO<sub>2</sub> effect in our reconstructions of  $\alpha$  because the change in CO<sub>2</sub> over the  
414 Holocene was only 40 ppm. This change relative to modern levels has only a small impact on  
415 the reconstructions (Prentice et al., 2022) and is sufficiently small to be within the  
416 reconstruction uncertainties. Furthermore, accounting for changes in CO<sub>2</sub> would not affect the  
417 reconstructed west-east gradient through time.

418 A more serious issue for our reconstructions may be the extent to which the vegetation cover  
419 of Iberia was substantially modified by human activities during the Holocene. Archaeological  
420 evidence shows that the introduction of agriculture during the Neolithic transition occurred ca  
421 7.6 ka in some southern and eastern areas of the Iberian Peninsula but spread slowly and  
422 farming first occurred only around 6 ka in the northwest (Drake et al., 2017; Fyfe et al., 2019;  
423 Zapata et al., 2004). Anthropogenic changes in land use have been detected at a number of  
424 sites, based on pollen evidence of increases in weeds or the presence of cereals (e.g. Abel-  
425 Schaad and López-Sáez, 2013; Cortés Sánchez et al., 2012; López-Merino et al., 2010; Mighall  
426 et al., 2006; Peña-Chocarro et al., 2005) or the presence of fungal spores associated with animal  
427 faeces which has been used to identify the presence of domesticated animals (e.g. López-Sáez  
428 and López-Merino, 2007; Revelles et al., 2018). The presence of cereals is the most reliable  
429 source of data on human activities, but most cereals only release pollen during threshing and  
430 thus are not found in abundance in pollen diagrams from natural (as opposed to archaeological)  
431 sites (Trondman et al., 2015). Indeed, it is only after ca 1 ka that the number of sites which  
432 record cereal pollen exceeds the number of sites at which cereals are not represented (Githumbi  
433 et al., 2022). Thus, while anthropogenic activities may have been important at the local scale  
434 and particularly in the later Holocene (e.g. Connor et al., 2019; Fyfe et al., 2019; Githumbi et  
435 al., 2022), most of the sites used for our reconstructions are not associated with archaeological  
436 evidence of agriculture or substantial landscape modification. Furthermore, the consistency of  
437 the reconstructed changes in climate across sites provides support for these being largely a  
438 reflection of regional climate changes rather than human activities.

439 We have used a modified version of fxTWA-PLS to reconstruct Holocene climates of the  
440 Iberian Peninsula because this modification reduced the compression bias in MTCO and  
441 MTWA, and specifically reduces the maximum bias in MTCO, MTWA and  $\alpha$ . Although this  
442 modified approach produces better overall reconstructions (Appendix A), its use does not  
443 change the reconstructed trends in these variables through time (SI Fig. S10). Thus, the finding  
444 that winter temperatures are a direct reflection of insolation forcing whereas summer

445 temperatures are influenced by land-surface feedbacks and changes in atmospheric circulation  
446 is robust to the version of fxTWA-PLS used. However, while we use a much larger data set  
447 than previous reconstructions, the distribution of pollen sites is uneven and the northern part  
448 of the Peninsula is better sampled than the southwest, which could lead to some uncertainties  
449 in the interpretation of changes in the west-east gradient of moisture. It would, therefore, be  
450 useful to specifically target the southwestern part of the Iberian Peninsula for new data  
451 collection. Alternatively, it would be useful to apply the approach used here to the whole of  
452 Eurasia, given that the failure of state-of-the-art climate models to advect moisture into the  
453 continental interior appears to be a feature of the whole region (Bartlein et al., 2017) and not  
454 the Peninsula alone.

455 **5. Conclusion**

456 We have developed an improved version of fxTWA-PLS which further reduces compression  
457 bias and provides robust climate reconstructions. We have used this technique with a large  
458 pollen data set representing 117 sites across the Iberian Peninsula to make quantitative  
459 reconstructions of summer and winter temperature and an index of plant-available moisture  
460 through the Holocene. We show that there was a gradual increase in winter temperature through  
461 the Holocene and that this trend broadly follows the changes in orbital forcing. Summer  
462 temperatures, however, do not follow the changes in orbital forcing but appear to be influenced  
463 by land-surface feedbacks associated with changes in moisture. We show that the west-east  
464 gradient in moisture was considerably less pronounced during the mid-Holocene (8~4 ka),  
465 implying a significant increase in moisture advection into the continental interior resulting from  
466 changes in circulation. Our reconstructions of temperature changes are broadly consistent with  
467 previous reconstructions, but are more solidly based because of the increased site coverage.  
468 Our reconstructions of changes in the west-east gradient of moisture during the early part of  
469 the Holocene are also consistent with previous reconstructions, although this change is not  
470 simulated by state-of-the-art climate models, implying that there are still issues to resolve the  
471 associated land-surface feedbacks in these models. Our work provides an improved foundation  
472 for documenting and understanding the Holocene palaeoclimates of Iberia.

473

474 **Data and Code Availability**

475 All the data used are public access and cited here. The code used to generate the climate  
476 reconstructions is available at <https://github.com/ml4418/Iberia-paper.git>.

477 **Supplement.** The supplement related to this article is available online.

478 **Competing interests.** We declare that we have no conflict of interest.

479 **Author Contributions.** ML, ICP and SPH designed the study. ML, ICP and CJFtB designed  
480 the modifications to fxTWA-PLS. PG-S and GG-R provided pollen data and insights into the  
481 regional palaeoclimate histories. ML carried out the analyses. ML and SPH wrote the first  
482 draft of the paper and all authors contributed to the final draft.

483 **Acknowledgements.** ML acknowledges support from Imperial College through the Lee  
484 Family Scholarship. YS and SPH acknowledge support from the ERC-funded project GC 2.0  
485 (Global Change 2.0: Unlocking the past for a clearer future; grant number 694481). ICP  
486 acknowledges support from the ERC under the European Union Horizon 2020 research and  
487 innovation programme (grant agreement no: 787203 REALM). This work is a contribution to  
488 the project "Origen y Cuantification de los Cambios Paleoambientales en el Pirineo:  
489 Variabilidad climatic e impacto humano" (PYCACHU: PID2019-106050RB-I00)" funded by  
490 the Ministerio de Ciencia e Innovación.

491 **Financial support.** This research has been supported by Lee Family Scholarship fund, and  
492 the European Research Council (grant no. GC2.0, 694481, and grant no. REALM, 787203).

493 **References**

494 Abel-Schaad, D. and López-Sáez, J. A.: Vegetation changes in relation to fire history and  
 495 human activities at the Peña Negra mire (Bejar Range, Iberian Central Mountain System,  
 496 Spain) during the past 4,000 years, *Veg. Hist. Archaeobot.*, 22, 199–214,  
 497 doi:10.1007/s00334-012-0368-9, 2013.

498 Allison, P. D.: *Multiple Regression: A Primer*, Pine Forge Press., 1994.

499 Andrade, C., Contente, J. and Santos, J. A.: Climate change projections of aridity conditions  
 500 in the Iberian Peninsula, *Water*, 13(15), doi:10.3390/w13152035, 2021a.

501 Andrade, C., Contente, J. and Santos, J. A.: Climate change projections of dry and wet events  
 502 in Iberia based on the WASP-Index, *Climate*, 9(6), doi:10.3390/cli9060094, 2021b.

503 Aranbarri, J., Gonzalez Samperiz, P., Valero-Garcés, B., Moreno, A., Gil-Romera, G.,  
 504 Sevilla-Callejo, M., García-Prieto, E., Di Rita, F., Mata, M. del Pi., Morellón, M., Magri, D.,  
 505 Rodríguez-Lázaro, J. and Carrión, J.: Rapid climatic changes and resilient vegetation during  
 506 the Lateglacial and Holocene in a continental region of south-western Europe, *Glob. Planet.  
 507 Change*, 114, 50–65, doi:10.1016/j.gloplacha.2014.01.003, 2014.

508 Aranbarri, J., González-Sampériz, P., Iriarte, E., Moreno, A., Rojo-Guerra, M., Peña-  
 509 Chocarro, L., Valero-Garcés, B., Leunda, M., García-Prieto, E., Sevilla-Callejo, M., Gil-  
 510 Romera, G., Magri, D. and Rodríguez-Lázaro, J.: Human–landscape interactions in the  
 511 Conquezuela–Ambrona Valley (Soria, continental Iberia): From the early Neolithic land use  
 512 to the origin of the current oak woodland, *Palaeogeogr. Palaeoclimatol. Palaeoecol.*, 436, 41–  
 513 57, doi:<https://doi.org/10.1016/j.palaeo.2015.06.030>, 2015.

514 Baldini, L. M., Baldini, J. U. L., McDermott, F., Arias, P., Cueto, M., Fairchild, I. J.,  
 515 Hoffmann, D. L., Mattey, D. P., Müller, W., Nita, D. C., Ontañón, R., Garcíá-Moncó, C. and  
 516 Richards, D. A.: North Iberian temperature and rainfall seasonality over the Younger Dryas  
 517 and Holocene, *Quat. Sci. Rev.*, 226, 105998,  
 518 doi:<https://doi.org/10.1016/j.quascirev.2019.105998>, 2019.

519 Bartlein, P. J., Prentice, I. C. and Webb, T.: Climatic response surfaces from pollen data for  
 520 some Eastern North American taxa, *J. Biogeogr.*, 13(1), 35, doi:10.2307/2844848, 1986.

521 Bartlein, P. J., Harrison, S. P., Brewer, S., Connor, S., Davis, B. A. S., Gajewski, K., Guiot,  
 522 J., Harrison-Prentice, T. I., Henderson, A., Peyron, O., Prentice, I. C., Scholze, M., Seppä, H.,  
 523 Shuman, B., Sugita, S., Thompson, R. S., Viau, A. E., Williams, J. and Wu, H.: Pollen-based  
 524 continental climate reconstructions at 6 and 21 ka: A global synthesis, *Clim. Dyn.*, 37(3),  
 525 775–802, doi:10.1007/s00382-010-0904-1, 2011.

526 Bartlein, P. J., Harrison, S. P. and Izumi, K.: Underlying causes of Eurasian midcontinental  
 527 aridity in simulations of mid-Holocene climate, *Geophys. Res. Lett.*, 44(17), 9020–9028,  
 528 doi:10.1002/2017GL074476, 2017.

529 Blaauw, M. and Christeny, J. A.: Flexible paleoclimate age-depth models using an  
 530 autoregressive gamma process, *Bayesian Anal.*, 6(3), 457–474, doi:10.1214/11-BA618, 2011.

531 Blaauw, M., Christen, J. A., Lopez, M. A. A. V., V., J. E. O. M. G., Belding, T., Theiler, J.,  
 532 Gough, B. and Karney, C.: *rbacon*: Age-depth modelling using Bayesian statistics, [online]  
 533 Available from: <https://cran.r-project.org/package=rbacon>, 2021.

534 ter Braak, C. J. F. and Juggins, S.: Weighted averaging partial least squares regression (WA-  
 535 PLS): An improved method for reconstructing environmental variables from species  
 536 assemblages, *Hydrobiologia*, 269(1), 485–502, doi:10.1007/BF00028046, 1993.

537 Braconnot, P., Crétat, J., Marti, O., Balkanski, Y., Caubel, A., Cozic, A., Foujols, M.-A. and  
 538 Sanogo, S.: Impact of multiscale variability on last 6,000 years Indian and West African  
 539 monsoon rain, *Geophys. Res. Lett.*, 46(23), 14021–14029,  
 540 doi:<https://doi.org/10.1029/2019GL084797>, 2019.

541 Brierley, C. M., Zhao, A., Harrison, S. P., Braconnot, P., Williams, C. J. R., Thornalley, D. J.  
 542 R., Shi, X., Peterschmitt, J.-Y., Ohgaito, R., Kaufman, D. S., Kageyama, M., Hargreaves, J.  
 543 C., Erb, M. P., Emile-Geay, J., D'Agostino, R., Chandan, D., Carré, M., Bartlein, P., Zheng,  
 544 W., Zhang, Z., Zhang, Q., Yang, H., Volodin, E. M., Tomas, R. A., Routson, C., Peltier, W.  
 545 R., Otto-Bliesner, B., Morozova, P. A., McKay, N. P., Lohmann, G., Legrande, A. N., Guo,  
 546 C., Cao, J., Brady, E., Annan, J. D. and Abe-Ouchi, A.: Large-scale features and evaluation  
 547 of the PMIP4-CMIP6 midHolocene simulations, *Clim. Past Discuss.*, 2020, 1–35,  
 548 doi:10.5194/cp-2019-168, 2020.

549 Camuera, J., Ramos-Román, M. J., Jiménez-Moreno, G., García-Alix, A., Ilvonen, L., Ruha,  
 550 L., Gil-Romera, G., González-Sampériz, P. and Seppä, H.: Past 200 kyr hydroclimate  
 551 variability in the western Mediterranean and its connection to the African Humid Periods,  
 552 *Sci. Rep.*, 12(1), 9050, doi:10.1038/s41598-022-12047-1, 2022.

553 Carré, M., Braconnot, P., Elliot, M., d'Agostino, R., Schurer, A., Shi, X., Marti, O.,  
 554 Lohmann, G., Jungclaus, J., Cheddadi, R., Abdelkader di Carlo, I., Cardich, J., Ochoa, D.,  
 555 Salas Gismondi, R., Pérez, A., Romero, P. E., Turcq, B., Corrège, T. and Harrison, S. P.:  
 556 High-resolution marine data and transient simulations support orbital forcing of ENSO  
 557 amplitude since the mid-Holocene, *Quat. Sci. Rev.*, 268, 107125,  
 558 doi:<https://doi.org/10.1016/j.quascirev.2021.107125>, 2021.

559 Carrión, J. S., Fernández, S., González-Sampériz, P., Gil-Romera, G., Badal, E., Carrión-  
 560 Marco, Y., López-Merino, L., López-Sáez, J. A., Fierro, E. and Burjachs, F.: Expected trends  
 561 and surprises in the Lateglacial and Holocene vegetation history of the Iberian Peninsula and  
 562 Balearic Islands, *Rev. Palaeobot. Palynol.*, 162(3), 458–475,  
 563 doi:<https://doi.org/10.1016/j.revpalbo.2009.12.007>, 2010.

564 Carrión, Y., Kaal, J., López-Sáez, J. A., López-Merino, L. and Martínez Cortizas, A.:  
 565 Holocene vegetation changes in NW Iberia revealed by anthracological and palynological  
 566 records from a colluvial soil, *The Holocene*, 20(1), 53–66, doi:10.1177/0959683609348849,  
 567 2009.

568 Carvalho, D., Pereira, S. and Rocha, A.: Future surface temperature changes for the Iberian  
 569 Peninsula according to EURO-CORDEX climate projections, *Clim. Dyn.*, 56, 1–16,  
 570 doi:10.1007/s00382-020-05472-3, 2021.

571 Cheddadi, R., Yu, G., Joel, G., Harrison, S., Prentice, I. and Colin, I.: The climate of Europe  
 572 6000 years ago, *Clim. Dyn.*, 13, 1, doi:10.1007/s003820050148, 1997.

573 Chevalier, M., Davis, B. A. S., Heiri, O., Seppä, H., Chase, B. M., Gajewski, K., Lacourse,  
 574 T., Telford, R. J., Finsinger, W., Guiot, J., Kühl, N., Maezumi, S. Y., Tipton, J. R., Carter, V.  
 575 A., Brussel, T., Phelps, L. N., Dawson, A., Zanon, M., Vallé, F., Nolan, C., Mauri, A., de  
 576 Vernal, A., Izumi, K., Holmström, L., Marsicek, J., Goring, S., Sommer, P. S., Chaput, M.  
 577 and Kupriyanov, D.: Pollen-based climate reconstruction techniques for late Quaternary  
 578 studies, *Earth-Science Rev.*, 210, 103384,  
 579 doi:<https://doi.org/10.1016/j.earscirev.2020.103384>, 2020.

580 Connor, S., Vannière, B., Colombaroli, D., Anderson, R., Carrión, J., Ejarque, A., Gil-  
 581 Romera, G., Gonzalez Samperiz, P., Höfer, D., Morales-Molino, C., Revelles, J., Schneider,  
 582 H., Knaap, W., Leeuwen, J. and Woodbridge, J.: Humans take control of fire-driven diversity  
 583 changes in Mediterranean Iberia's vegetation during the mid–late Holocene, *The Holocene*,  
 584 29, 095968361982665, doi:10.1177/0959683619826652, 2019.

585 Cortés Sánchez, M., Jiménez Espejo, F. J., Simón Vallejo, M. D., Gibaja Bao, J. F., Carvalho,  
 586 A. F., Martínez-Ruiz, F., Gamiz, M. R., Flores, J.-A., Paytan, A., López Sáez, J. A., Peña-  
 587 Chocarro, L., Carrión, J. S., Morales Muñiz, A., Roselló Izquierdo, E., Riquelme Cantal, J.  
 588 A., Dean, R. M., Salgueiro, E., Martínez Sánchez, R. M., De la Rubia de Gracia, J. J., Lozano  
 589 Francisco, M. C., Vera Peláez, J. L., Rodríguez, L. L. and Bicho, N. F.: The Mesolithic–  
 590 Neolithic transition in southern Iberia, *Quat. Res.*, 77(2), 221–234,  
 591 doi:<https://doi.org/10.1016/j.yqres.2011.12.003>, 2012.

592 Dallmeyer, A., Claussen, M., Lorenz, S. J. and Shanahan, T.: The end of the African humid  
 593 period as seen by a transient comprehensive Earth system model simulation of the last 8000  
 594 years, , doi:10.5194/cp-2019-86, 2020.

595 Davis, B. A. S., Brewer, S., Stevenson, A. C. and Guiot, J.: The temperature of Europe during  
 596 the Holocene reconstructed from pollen data, *Quat. Sci. Rev.*, 22(15), 1701–1716,  
 597 doi:[https://doi.org/10.1016/S0277-3791\(03\)00173-2](https://doi.org/10.1016/S0277-3791(03)00173-2), 2003.

598 Davis, T. W., Prentice, I. C., Stocker, B. D., Thomas, R. T., Whitley, R. J., Wang, H., Evans,  
 599 B. J., Gallego-Sala, A. V., Sykes, M. T. and Cramer, W.: Simple process-led algorithms for  
 600 simulating habitats (SPLASH v.1.0): Robust indices of radiation, evapotranspiration and  
 601 plant-available moisture, *Geosci. Model Dev.*, 10(2), 689–708, doi:10.5194/gmd-10-689-  
 602 2017, 2017.

603 Drake, B. L., Blanco-González, A. and Lillios, K. T.: Regional Demographic Dynamics in  
 604 the Neolithic Transition in Iberia: Results from Summed Calibrated Date Analysis, *J.  
 605 Archaeol. Method Theory*, 24(3), 796–812, doi:10.1007/s10816-016-9286-y, 2017.

606 Eilers, P. H. and Marx, B. D.: Practical smoothing: The Joys of P-splines, edited by P. H.  
 607 Eilers and B. D. Marx, Cambridge University Press., 2021.

608 Farquhar, G. D.: Carbon dioxide and vegetation, *Science* (80-.), 278(5342), 1411,  
 609 doi:10.1126/science.278.5342.1411, 1997.

610 Fyfe, R. M., Woodbridge, J., Palmisano, A., Bevan, A., Shennan, S., Burjachs, F., Legarra  
 611 Herrero, B., García Puchol, O., Carrión, J. S., Revelles, J. and Roberts, C. N.: Prehistoric  
 612 palaeodemographics and regional land cover change in eastern Iberia, *Holocene*, 29(5), 799–  
 613 815, doi:10.1177/0959683619826643, 2019.

614 García-Alix, A., Camuera, J., Ramos-Román, M. J., Toney, J. L., Sachse, D., Schefuß, E.,  
 615 Jiménez-Moreno, G., Jiménez-Espejo, F. J., López-Avilés, A., Anderson, R. S. and Yanes,  
 616 Y.: Paleohydrological dynamics in the Western Mediterranean during the last glacial cycle,  
 617 *Glob. Planet. Change*, 202, 103527, doi:<https://doi.org/10.1016/j.gloplacha.2021.103527>,  
 618 2021.

619 Gerhart, L. M. and Ward, J. K.: Plant responses to low [CO<sub>2</sub>] of the past, *New Phytol.*,  
 620 188(3), 674–695, doi:<https://doi.org/10.1111/j.1469-8137.2010.03441.x>, 2010.

621 Githumbi, E., Fyfe, R., Gaillard, M.-J., Trondman, A.-K., Mazier, F., Nielsen, A.-B., Poska,  
 622 A., Sugita, S., Woodbridge, J., Azuara, J., Feurdean, A., Grindean, R., Lebreton, V.,  
 623 Marquer, L., Nebout-Combourieu, N., Stančikaitė, M., Tančūau, I., Tonkov, S.,  
 624 Shumilovskikh, L. and data contributors, L.: European pollen-based REVEALS land-cover  
 625 reconstructions for the Holocene: methodology, mapping and potentials, *Earth Syst. Sci.  
 626 Data*, 14(4), 1581–1619, doi:10.5194/essd-14-1581-2022, 2022.

627 González-Sampériz, P., Aranbarri, J., Pérez-Sanz, A., Gil-Romera, G., Moreno, A., Leunda,  
 628 M., Sevilla-Callejo, M., Corella, J. P., Morellón, M., Oliva, B. and Valero-Garcés, B.:  
 629 Environmental and climate change in the southern Central Pyrenees since the Last Glacial  
 630 Maximum: A view from the lake records, *Catena*, 149, 668–688,  
 631 doi:<https://doi.org/10.1016/j.catena.2016.07.041>, 2017.

632 Granados, I. and Toro, M.: Recent warming in a high mountain lake (Laguna Cimera, Central  
 633 Spain) inferred by means of fossil chironomids, *J. Limnol.*, 59 (suppl., 109–119,  
 634 doi:10.4081/limnol.2000.s1.109, 2000.

635 Hammer, O., Harper, D. and Ryan, P.: PAST: Paleontological statistics software package for  
 636 education and data analysis, *Palaeontol. Electron.*, 4, 1–9, 2001.

637 Harrison, S., Shen, Y. and Sweeney, L.: Pollen data and charcoal data of the Iberian  
 638 Peninsula (version 3), [online] Available from: <https://doi.org/10.17864/1947.000369>, 2022.

639 Harrison, S. P.: Modern pollen data for climate reconstructions, version 1 (SMPDS), ,  
 640 doi:<http://dx.doi.org/10.17864/1947.194>, 2019.

641 Harrison, S. P., Prentice, I. C., Barboni, D., Kohfeld, K. E., Ni, J. and Sutra, J.-P.:

642 Ecophysiological and bioclimatic foundations for a global plant functional classification, J.  
 643 *Veg. Sci.*, 21(2), 300–317, doi:10.1111/j.1654-1103.2009.01144.x, 2010.

644 Holden, P. B., Birks, H. J. B., Brooks, S. J., Bush, M. B., Hwang, G. M., Matthews-Bird, F.,  
 645 Valencia, B. G. and van Woesik, R.: BUMPER v1.0: a Bayesian user-friendly model for  
 646 palaeo-environmental reconstruction, *Geosci. Model Dev.*, 10(1), 483–498,  
 647 doi:10.5194/gmd-10-483-2017, 2017.

648 Ilvonen, L., López-Sáez, J. A., Holmström, L., Alba-Sánchez, F., Pérez-Díaz, S., Carrión, J.  
 649 S., Ramos-Román, M. J., Camuera, J., Jiménez-Moreno, G., Ruha, L. and Seppä, H.: Spatial  
 650 and temporal patterns of Holocene precipitation change in the Iberian Peninsula, *Boreas*,  
 651 doi:<https://doi.org/10.1111/bor.12586>, 2022.

652 Jiang, W., GUIOT, J., CHU, G., WU, H., YUAN, B., HATTÉ, C. and GUO, Z.: An improved  
 653 methodology of the modern analogues technique for palaeoclimate reconstruction in arid and  
 654 semi-arid regions, *Boreas*, 39(1), 145–153, doi:<https://doi.org/10.1111/j.1502-3885.2009.00115.x>, 2010.

655 Kaufman, D., McKay, N., Routson, C., Erb, M., Davis, B., Heiri, O., Jaccard, S., Tierney, J.,  
 656 Dätwyler, C., Axford, Y., Brussel, T., Cartapanis, O., Chase, B., Dawson, A., de Vernal, A.,  
 657 Engels, S., Jonkers, L., Marsicek, J., Moffa-Sánchez, P., Morrill, C., Orsi, A., Rehfeld, K.,  
 658 Saunders, K., Sommer, P. S., Thomas, E., Tonello, M., Tóth, M., Vachula, R., Andreev, A.,  
 659 Bertrand, S., Biskaborn, B., Bringué, M., Brooks, S., Caniupán, M., Chevalier, M., Cwynar,  
 660 L., Emile-Geay, J., Fegyveresi, J., Feurdean, A., Finsinger, W., Fortin, M.-C., Foster, L., Fox,  
 661 M., Gajewski, K., Grosjean, M., Hausmann, S., Heinrichs, M., Holmes, N., Ilyashuk, B.,  
 662 Ilyashuk, E., Juggins, S., Khider, D., Koinig, K., Langdon, P., Larocque-Tobler, I., Li, J.,  
 663 Lotter, A., Luoto, T., Mackay, A., Magyari, E., Malevich, S., Mark, B., Massaferro, J.,  
 664 Montade, V., Nazarova, L., Novenko, E., Paril, P., Pearson, E., Peros, M., Pienitz, R.,  
 665 Płociennik, M., Porinchu, D., Potito, A., Rees, A., Reinemann, S., Roberts, S., Rolland, N.,  
 666 Salonen, S., Self, A., Seppä, H., Shala, S., St-Jacques, J.-M., Stenni, B., Syrykh, L., Tarrats,  
 667 P., Taylor, K., van den Bos, V., Velle, G., Wahl, E., Walker, I., Wilmshurst, J., Zhang, E. and  
 668 Zhilich, S.: A global database of Holocene paleotemperature records, *Sci. Data*, 7(1), 115,  
 669 doi:10.1038/s41597-020-0445-3, 2020.

670

671 Liu, M., Prentice, I. C., ter Braak, C. J. F. and Harrison, S. P.: An improved statistical  
 672 approach for reconstructing past climates from biotic assemblages, *Proc. R. Soc. A Math.*,  
 673 476(2243), doi:<https://doi.org/10.1098/rspa.2020.0346>, 2020.

674 López-Merino, L., Cortizas, A. M. and López-Sáez, J. A.: Early agriculture and  
 675 palaeoenvironmental history in the North of the Iberian Peninsula: a multi-proxy analysis of  
 676 the Monte Areo mire (Asturias, Spain), *J. Archaeol. Sci.*, 37(8), 1978–1988,  
 677 doi:<https://doi.org/10.1016/j.jas.2010.03.003>, 2010.

678 López-Sáez, J. A. and López-Merino, L.: Coprophilous fungi as a source of information of  
 679 anthropic activities during the Prehistory in the Amblés Valley (Ávila, Spain): The  
 680 archaeopaleontological record, *Rev. Española Micropaleontol.*, 38, 49–75, 2007.

681 Martínez-Cortizas, A., Costa-Casais, M. and López-Sáez, J. A.: Environmental change in

682 NW Iberia between 7000 and 500cal BC, *Quat. Int.*, 200(1), 77–89,  
 683 doi:<https://doi.org/10.1016/j.quaint.2008.07.012>, 2009.

684 Mauri, A., Davis, B. A. S., Collins, P. M. and Kaplan, J. O.: The influence of atmospheric  
 685 circulation on the mid-Holocene climate of Europe: a data–model comparison, *Clim. Past*,  
 686 10(5), 1925–1938, doi:10.5194/cp-10-1925-2014, 2014.

687 Mauri, A., Davis, B. A. S., Collins, P. M. and Kaplan, J. O.: The climate of Europe during the  
 688 Holocene: A gridded pollen-based reconstruction and its multi-proxy evaluation, *Quat. Sci.*  
 689 *Rev.*, 112, 109–127, doi:10.1016/j.quascirev.2015.01.013, 2015.

690 Mighall, T. M., Martínez Cortizas, A., Biester, H. and Turner, S. E.: Proxy climate and  
 691 vegetation changes during the last five millennia in NW Iberia: Pollen and non-pollen  
 692 palynomorph data from two ombrotrophic peat bogs in the North Western Iberian Peninsula,  
 693 *Rev. Palaeobot. Palynol.*, 141(1–2), 203–223, doi:10.1016/j.revpalbo.2006.03.013, 2006.

694 Millet, L., Rius, D., Galop, D., Heiri, O. and Brooks, S. J.: Chironomid-based reconstruction  
 695 of Lateglacial summer temperatures from the Ech palaeolake record (French western  
 696 Pyrenees), *Palaeogeogr. Palaeoclimatol. Palaeoecol.*, 315–316, 86–99,  
 697 doi:<https://doi.org/10.1016/j.palaeo.2011.11.014>, 2012.

698 Morellón, M., Aranbarri, J., Moreno, A., González-Sampériz, P. and Valero-Garcés, B. L.:  
 699 Early Holocene humidity patterns in the Iberian Peninsula reconstructed from lake, pollen  
 700 and speleothem records, *Quat. Sci. Rev.*, 181, 1–18,  
 701 doi:<https://doi.org/10.1016/j.quascirev.2017.11.016>, 2018.

702 Muñoz Sobrino, C., Heiri, O., Hazekamp, M., van der Velden, D., Kirilova, E. P., García-  
 703 Moreiras, I. and Lotter, A. F.: New data on the Lateglacial period of SW Europe: a high  
 704 resolution multiproxy record from Laguna de la Roya (NW Iberia), *Quat. Sci. Rev.*, 80, 58–  
 705 77, doi:<https://doi.org/10.1016/j.quascirev.2013.08.016>, 2013.

706 New, M., Lister, D. and Hulme, M.: A high-resolution data set of surface climate over global  
 707 land areas , *Clim. Res.*, 21(1), 1–25 [online] Available from: <http://www.int-res.com/abstracts/cr/v21/n1/p1-25/>, 2002.

709 Overpeck, J. T., Webb, T. and Prentice, I. C.: Quantitative interpretation of fossil pollen  
 710 spectra: Dissimilarity coefficients and the method of modern analogs, *Quat. Res.*, 23(1), 87–  
 711 108, doi:10.1016/0033-5894(85)90074-2, 1985.

712 Parker, S. E., Harrison, S. P. and Braconnot, P.: Speleothem records of monsoon interannual-  
 713 interdecadal variability through the Holocene, *Environ. Res. Commun.*, 3(12), 121002,  
 714 doi:10.1088/2515-7620/ac3eaa, 2021.

715 Peña-Chocarro, L., Peña, L. Z., Gazolaz, J. G., Morales, M. G., Sesma, J. S. and Straus, L.  
 716 G.: The spread of agriculture in northern Iberia: new archaeobotanical data from El Mirón  
 717 cave (Cantabria) and the open-air site of Los Cascajos (Navarra), *Veg. Hist. Archaeobot.*,  
 718 14(4), 268–278, doi:10.1007/s00334-005-0078-7, 2005.

719 Peyron, O., Guiot, J., Cheddadi, R., Tarasov, P., Reille, M., de Beaulieu, J.-L., Bottema, S.  
 720 and Andrieu, V.: Climatic reconstruction in Europe for 18,000 yr B.P. from pollen data, *Quat.*  
 721 *Res.*, 49(2), 183–196, doi:<https://doi.org/10.1006/qres.1997.1961>, 1998.

722 Prentice, I. C. and Harrison, S. P.: Ecosystem effects of CO<sub>2</sub> concentration: evidence from  
 723 past climates, *Clim. Past*, 5(3), 297–307, doi:10.5194/cp-5-297-2009, 2009.

724 Prentice, I. C., Meng, T., Wang, H., Harrison, S. P., Ni, J. and Wang, G.: Evidence of a  
 725 universal scaling relationship for leaf CO<sub>2</sub> drawdown along an aridity gradient, *New Phytol.*,  
 726 190(1), 169–180, doi:<https://doi.org/10.1111/j.1469-8137.2010.03579.x>, 2011.

727 Prentice, I. C., Cleator, S. F., Huang, Y. H., Harrison, S. P. and Roulstone, I.: Reconstructing  
 728 ice-age palaeoclimates: Quantifying low-CO<sub>2</sub> effects on plants, *Glob. Planet. Change*, 149,  
 729 166–176, doi:<https://doi.org/10.1016/j.gloplacha.2016.12.012>, 2017.

730 Prentice, I. C., Villegas-Diaz, R. and Harrison, S. P.: Accounting for atmospheric carbon  
 731 dioxide variations in pollen-based reconstruction of past hydroclimates, *Glob. Planet.*  
 732 *Change*, 2022.

733 Ramos-Román, M. J., Jiménez-Moreno, G., Camuera, J., García-Alix, A., Anderson, R.,  
 734 Jiménez-Espejo, F., Sachse, D., Jaime, T., Carrión, J., Webster, C. and Yanes, Y.: Millennial-  
 735 scale cyclical environment and climate variability during the Holocene in the western  
 736 Mediterranean region deduced from a new multi-proxy analysis from the Padul record (Sierra  
 737 Nevada, Spain), *Glob. Planet. Change*, 168, doi:10.1016/j.gloplacha.2018.06.003, 2018.

738 Reimer, P. J., Austin, W. E. N., Bard, E., Bayliss, A., Blackwell, P. G., Bronk Ramsey, C.,  
 739 Butzin, M., Cheng, H., Edwards, R. L., Friedrich, M., Grootes, P. M., Guilderson, T. P.,  
 740 Hajdas, I., Heaton, T. J., Hogg, A. G., Hughen, K. A., Kromer, B., Manning, S. W.,  
 741 Muscheler, R., Palmer, J. G., Pearson, C., Van Der Plicht, J., Reimer, R. W., Richards, D. A.,  
 742 Scott, E. M., Southon, J. R., Turney, C. S. M., Wacker, L., Adolphi, F., Büntgen, U., Capano,  
 743 M., Fahrni, S. M., Fogtmann-Schulz, A., Friedrich, R., Köhler, P., Kudsk, S., Miyake, F.,  
 744 Olsen, J., Reinig, F., Sakamoto, M., Sookdeo, A. and Talamo, S.: The IntCal20 Northern  
 745 Hemisphere radiocarbon age calibration curve (0–55 cal kBP), *Radiocarbon*, 62(4), 725–757,  
 746 doi:10.1017/RDC.2020.41, 2020.

747 Revelles, J., Burjachs, F., Palomo, A., Piqué, R., Iriarte, E., Pérez-Obiol, R. and Terradas, X.:  
 748 Human-environment interaction during the Mesolithic- Neolithic transition in the NE Iberian  
 749 Peninsula. Vegetation history, climate change and human impact during the Early-Middle  
 750 Holocene in the Eastern Pre-Pyrenees, *Quat. Sci. Rev.*, 184, 183–200,  
 751 doi:<https://doi.org/10.1016/j.quascirev.2017.08.025>, 2018.

752 Salonen, J. S., Ilvonen, L., Seppä, H., Holmström, L., Telford, R. J., Gaidamavičius, A.,  
 753 Stančikaitė, M. and Subetto, D.: Comparing different calibration methods (WA/WA-PLS  
 754 regression and Bayesian modelling) and different-sized calibration sets in pollen-based  
 755 quantitative climate reconstruction, *The Holocene*, 22(4), 413–424,  
 756 doi:10.1177/0959683611425548, 2011.

757 Salonen, J. S., Korpela, M., Williams, J. W. and Luoto, M.: Machine-learning based  
 758 reconstructions of primary and secondary climate variables from North American and  
 759 European fossil pollen data, *Sci. Rep.*, 9(1), 15805, doi:10.1038/s41598-019-52293-4, 2019.

760 Schröder, T., López-Sáez, J. A., van't Hoff, J. and Reicherter, K.: Unravelling the Holocene  
 761 environmental history of south-western Iberia through a palynological study of Lake Medina  
 762 sediments, *The Holocene*, 30(1), 13–22, doi:10.1177/0959683619865590, 2019.

763 Shen, Y., Sweeney, L., Liu, M., Lopez Saez, J. A., Pérez-Díaz, S., Luelmo-Lautenschlaeger,  
 764 R., Gil-Romera, G., Hoefer, D., Jiménez-Moreno, G., Schneider, H., Prentice, I. C. and  
 765 Harrison, S. P.: Reconstructing burnt area during the Holocene: an Iberian case study, *Clim.*  
 766 *Past*, 18, 1189–1201, doi:10.5194/cp-2021-36, 2022.

767 Stoll, H. M., Moreno, A., Mendez-Vicente, A., Gonzalez-Lemos, S., Jimenez-Sanchez, M.,  
 768 Dominguez-Cuesta, M. J., Edwards, R. L., Cheng, H. and Wang, X.: Paleoclimate and  
 769 growth rates of speleothems in the northwestern Iberian Peninsula over the last two glacial  
 770 cycles, *Quat. Res.*, 80, 284–290, doi:10.1016/j.yqres.2013.05.002, 2013.

771 Tarrats, P., Heiri, O., Valero-Garcés, B., Cañedo-Argüelles, M., Prat, N., Rieradevall, M. and  
 772 González-Sampériz, P.: Chironomid-inferred Holocene temperature reconstruction in Basa de  
 773 la Mora Lake (Central Pyrenees), *The Holocene*, 28(11), 1685–1696,  
 774 doi:10.1177/0959683618788662, 2018.

775 Tarroso, P., Carrión, J., Dorado-Valiño, M., Queiroz, P., Santos, L., Valdeolmillos-  
 776 Rodríguez, A., Célio Alves, P., Brito, J. C. and Cheddadi, R.: Spatial climate dynamics in the  
 777 Iberian Peninsula since 15 000 yr BP, *Clim. Past*, 12(5), 1137–1149, doi:10.5194/cp-12-  
 778 1137-2016, 2016.

779 Thatcher, D. L., Wanamaker, A. D., Denniston, R. F., Asmerom, Y., Polyak, V. J., Fullick,  
 780 D., Ummenhofer, C. C., Gillikin, D. P. and Haws, J. A.: Hydroclimate variability from  
 781 western Iberia (Portugal) during the Holocene: Insights from a composite stalagmite isotope  
 782 record, *The Holocene*, 30(7), 966–981, doi:<https://doi.org/10.1177/0959683620908648>,  
 783 2020.

784 Trondman, A.-K., Gaillard, M.-J., Mazier, F., Sugita, S., Fyfe, R., Nielsen, A. B., Twiddle,  
 785 C., Barratt, P., Birks, H. J. B., Bjune, A. E., Björkman, L., Broström, A., Caseldine, C.,  
 786 David, R., Dodson, J., Dörfler, W., Fischer, E., van Geel, B., Giesecke, T., Hultberg, T.,  
 787 Kalnina, L., Kangur, M., van der Knaap, P., Koff, T., Kuneš, P., Lagerås, P., Latałowa, M.,  
 788 Lechterbeck, J., Leroyer, C., Leydet, M., Lindbladh, M., Marquer, L., Mitchell, F. J. G.,  
 789 Odgaard, B. V., Peglar, S. M., Persson, T., Poska, A., Rösch, M., Seppä, H., Veski, S. and  
 790 Wick, L.: Pollen-based quantitative reconstructions of Holocene regional vegetation cover  
 791 (plant-functional types and land-cover types) in Europe suitable for climate modelling, *Glob.*  
 792 *Chang. Biol.*, 21(2), 676–697, doi:<https://doi.org/10.1111/gcb.12737>, 2015.

793 Villegas-Díaz, Roberto; Cruz-Silva, Esmeralda; Harrison, S. P.: ageR: Supervised age  
 794 models, , doi:10.5281/zenodo.4636715, 2021.

795 Walczak, I. W., Baldini, J. U. L., Baldini, L. M., McDermott, F., Marsden, S., Standish, C.  
796 D., Richards, D. A., Andreo, B. and Slater, J.: Reconstructing high-resolution climate using  
797 CT scanning of unsectioned stalagmites: A case study identifying the mid-Holocene onset of  
798 the Mediterranean climate in southern Iberia, *Quat. Sci. Rev.*, 127, 117–128,  
799 doi:<https://doi.org/10.1016/j.quascirev.2015.06.013>, 2015.

800 Wei, D., González-Sampériz, P., Gil-Romera, G., Harrison, S. P. and Prentice, I. C.: Seasonal  
801 temperature and moisture changes in interior semi-arid Spain from the last interglacial to the  
802 Late Holocene, *Quat. Res.*, 101, 143–155, doi:DOI: 10.1017/qua.2020.108, 2021.

803 Wu, H., Guiot, J., Brewer, S. and Guo, Z.: Climatic changes in Eurasia and Africa at the last  
804 glacial maximum and mid-Holocene: reconstruction from pollen data using inverse  
805 vegetation modelling, *Clim. Dyn.*, 29(2), 211–229, doi:10.1007/s00382-007-0231-3, 2007.

806 Zapata, L., Peña-Chocarro, L., Pérez-Jordá, G. and Stika, H.-P.: Early Neolithic Agriculture  
807 in the Iberian Peninsula, *J. World Prehistory*, 18(4), 283–325 [online] Available from:  
808 <http://www.jstor.org/stable/25801225>, 2004.

809 Zhang, Y., Kong, Z., Ni, J., Yan, S. and Yang, Z.: Late Holocene palaeoenvironment change  
810 in central Tianshan of Xinjiang, northwest China, *Grana*, 46(3), 197–213,  
811 doi:10.1080/00173130701564748, 2007.

812

813 **Figure and Table Captions**

814 Figure 1. Climate space represented by mean temperature of the coldest month (MTCO),  
 815 mean temperature of the warmest month (MTWA), and plant-available moisture as  
 816 represented by  $\alpha$ , an estimate of the ratio of actual evapotranspiration to equilibrium  
 817 evapotranspiration. The grey points show climate values for a rectangular area ( $21^{\circ}$  W  $\sim$   $150^{\circ}$   
 818 E,  $29^{\circ}$  N  $\sim$   $82^{\circ}$  N) enclosing the SMPDS data set, derived from the Climate Research Unit  
 819 CRU CL 2.0 database (New et al., 2002). The black points show climate values of the  
 820 SMPDS dataset. The red points show climate values of the Iberian Peninsula region in the  
 821 SMPDS dataset.

822 Figure 2. Map showing the location of the 117 fossil sites in the Iberian Peninsula used for  
 823 climate reconstructions. Sites lower than 1000 m a.s.l. are shown as squares, sites higher than  
 824 1000 m a.s.l. are shown as triangles. The base maps show modern (a) mean temperature of  
 825 the coldest month (MTCO), (b) mean temperature of the warmest month (MTWA), and (c)  
 826 plant-available moisture as represented by  $\alpha$ , an estimate of the ratio of actual  
 827 evapotranspiration to equilibrium evapotranspiration.

828 Figure 3. Reconstructed anomalies in climate at individual sites through time. The sites are  
 829 grouped into high ( $>1000$ m) and low ( $<1000$ m) elevation sites and organised from west to east.  
 830 Grey cells indicate periods or longitudes with no data. The individual plots show the anomalies  
 831 in reconstructed (a,d) mean temperature of the coldest month (MTCO), (b,e) mean temperature  
 832 of the warmest month (MTWA), and (c,f) plant-available moisture as represented by  $\alpha$ , an  
 833 estimate of the ratio of actual evapotranspiration to equilibrium evapotranspiration. The  
 834 anomalies are expressed as deviations of the mean value in each bin ( $\pm 500$  years) from the  
 835 value at 0.5 ka at each site.

836 Figure 4. Reconstructed composite changes (anomalies to 0.5 ka) in (a) mean temperature of  
 837 the coldest month (MTCO), (b) mean temperature of the warmest month (MTWA) and (c)  
 838 plant-available moisture as represented by  $\alpha$ , through the Holocene compared to changes in  
 839 (d) winter and (e) summer insolation for the latitude of the Iberian Peninsula, using  $\pm 500$   
 840 years as the bin. The black lines show mean values across sites, with vertical line segments  
 841 showing the standard deviations of mean values using 1000 bootstrap cycles of site  
 842 resampling.

843 Figure 5. Changes in the west-east gradient of plant-available moisture as represented by  
 844 anomalies in  $\alpha$  relative to 0.5 ka at individual sites through the Holocene. The red lines show  
 845 the regression lines. The shades indicate the 95 % confidence intervals of the regression lines

846 Figure 6. The relationship between mean temperature of the warmest month (MTWA) and  
 847 plant-available moisture as represented by  $\alpha$  (a) in the modern climate data set, and (b) in the  
 848 Holocene reconstructions.

849 Figure 7. Comparison between reconstructed composite changes in climate anomalies. The first  
 850 column represents this paper, the second column represents Mauri et al. (2015), the third  
 851 column represents Kaufman et al. (2020), the fourth column represents Tarroso et al. (2016).  
 852 The composite curves from this paper and Kaufman et al. (2020) are calculated from individual  
 853 reconstructions, using anomalies to 0.5 ka and a bin of  $\pm 500$  years (time slices are 0.5, 1.5, ...,  
 854 11.5 ka). The composite curves from Mauri et al. (2015) are converted directly from the gridded  
 855 time slices which are provided with anomalies to 0.1 ka and a bin of  $\pm 500$  years (time slices  
 856 are 1, 2, ..., 12 ka). The composite curves from Tarroso et al. (2016) are also converted directly  
 857 from the gridded time slices provided, with anomalies to 0.5 ka and a bin of  $\pm 500$  years (time  
 858 slices are 3, 4, ..., 12 ka). Note that Tarroso et al. (2016) applied a smoothing to the data such  
 859 that the plots in the paper do not show the excursion in MTWA at 8 ka. In all of the plots, the  
 860 black lines show mean values across sites, with vertical line bars showing the standard  
 861 deviation of mean values using 1000 bootstrap cycles of site/grid resampling.

862 Figure 8. Simulated mean values of mean temperature of the coldest month (MTCO), mean  
 863 temperature of the warmest month (MTWA) and mean daily precipitation in Iberian Peninsula  
 864 between 8 ka and 0 ka, smoothed using 100 year bins. Here BP means before 1950 AD. The  
 865 black lines represent Max Planck Institute Earth System Model (MPI) simulations, the red lines  
 866 represent Alfred Wagner Institute Earth System Model (AWI) simulations, the blue lines  
 867 represent Institut Pierre Simon Laplace Climate Model (IPSL-CM5) TR5AS simulations, the  
 868 orange lines represent Institut Pierre Simon Laplace Climate Model (IPSL-CM6) TR6AV  
 869 simulations. The four simulations were forced by evolving orbital parameters and greenhouse  
 870 gas concentrations. The four models have different spatial resolution, with the finest resolution  
 871 being  $1.875^\circ \times 1.875^\circ$  (AWI, MPI) and the coarsest resolution being  $1.875^\circ \times 3.75^\circ$  (IPSL-  
 872 CM5, TR5AS).

873 Table 1. Details of the fossil pollen sites used. The fossil pollen data from the Iberian  
 874 Peninsula were compiled by Shen et al. (2021) and obtained from  
 875 <https://doi.org/10.17864/1947.000343>. The reference list of this table can be found in the  
 876 supplementary.

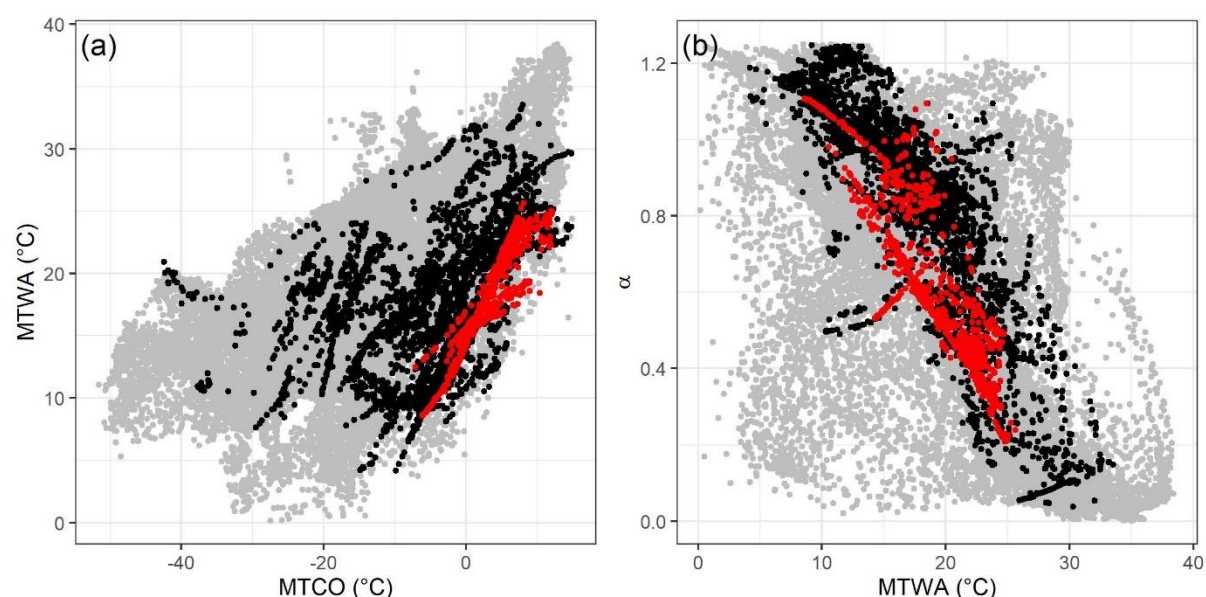
877 Table 2. Leave-out cross-validation (with geographically and climatically close sites  
 878 removed) fitness of the modified version of fxTWA-PLS, for mean temperature of the coldest  
 879 month (MTCO), mean temperature of the warmest month (MTWA) and plant-available  
 880 moisture ( $\alpha$ ), with p-spline smoothed fx estimation, using bins of 0.02, 0.02 and 0.002,  
 881 showing results for all the components. RMSEP is the root-mean-square error of prediction.

882  $\Delta$ RMSEP is the per cent change of RMSEP using the current number of components than  
883 using one component less.  $p$  assesses whether using the current number of components is  
884 significantly different from using one component less, which is used to choose the last  
885 significant number of components (indicated in bold) to avoid over-fitting. The degree of  
886 overall compression is assessed by linear regression of the cross-validated reconstructions  
887 onto the climate variable,  $b1$ ,  $b1.se$  are the slope and the standard error of the slope,  
888 respectively. The closer the slope ( $b1$ ) is to 1, the less the overall compression is.

889 Table 3. Canonical Correspondence Analysis (CCA) result of modern and fossil-  
890 reconstructed MTCO, MTWA and  $\alpha$ . The summary statistics for the ANOVA-like  
891 permutation test (999 permutations) are also shown. VIF is the variance inflation factor, Df is  
892 the number of degrees of freedom,  $\chi^2$  is the constrained eigenvalue (or the sum of constrained  
893 eigenvalues for the whole model), F is significance, and Pr (>F) is the probability. The CCA  
894 plots can be found in the Supplementary (Fig. S11).

895 Table 4. Assessment of the significance of anomalies to 0.5 ka through time with latitude and  
896 elevation. The slope is obtained by linear regression of the anomaly onto the longitude or  
897 elevation.  $p$  is the significance of the slope (bold parts:  $p < 0.05$ ).  $x_0$  is the point where the  
898 anomaly is 0 in the linear equation, which indicates longitude or elevation where the anomaly  
899 changes sign.

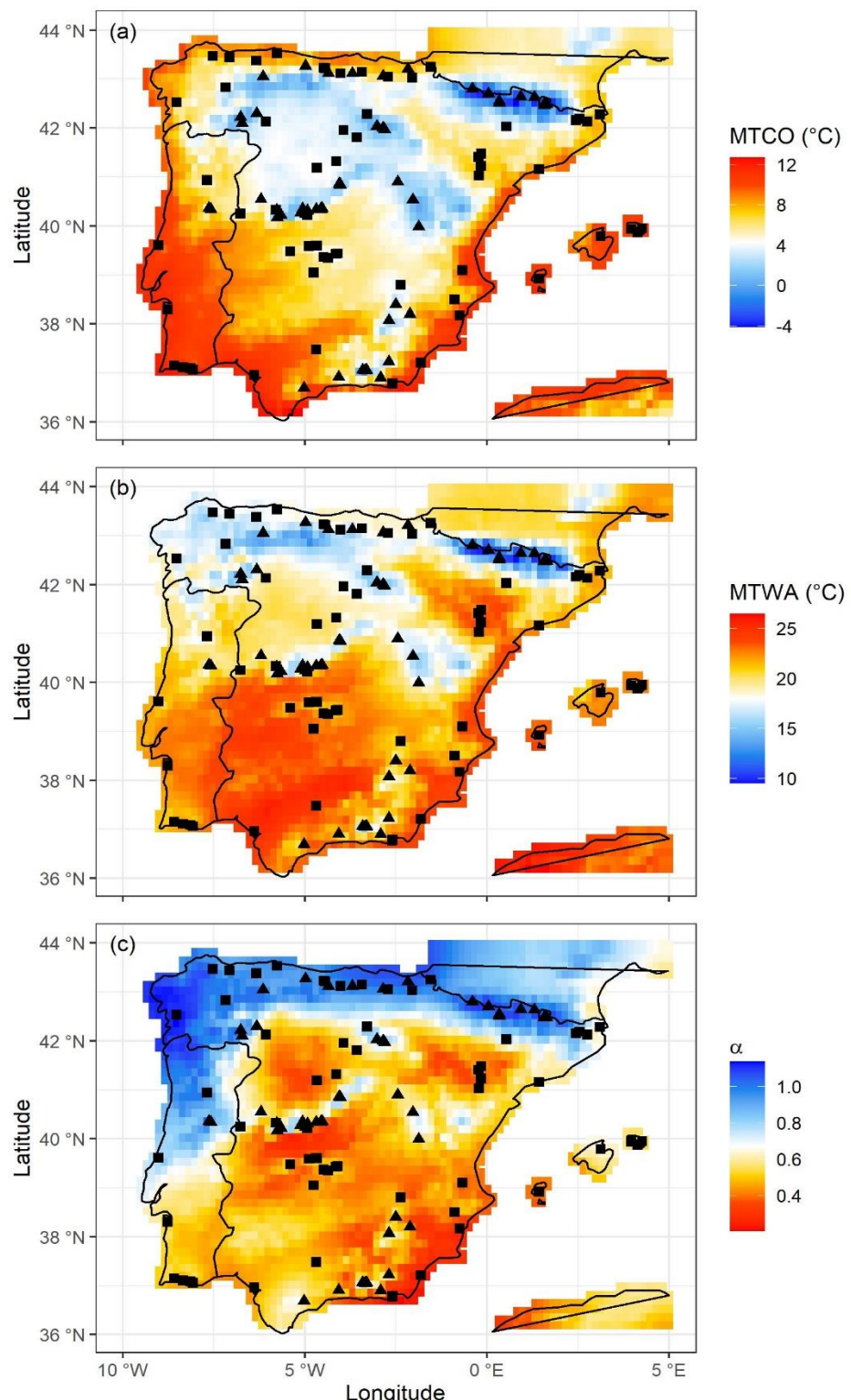
900 Figure 1. Climate space represented by mean temperature of the coldest month (MTCO),  
 901 mean temperature of the warmest month (MTWA), and plant-available moisture as  
 902 represented by  $\alpha$ , an estimate of the ratio of actual evapotranspiration to equilibrium  
 903 evapotranspiration. The grey points show climate values for a rectangular area ( $21^{\circ}$  W  $\sim$   $150^{\circ}$   
 904 E,  $29^{\circ}$  N  $\sim$   $82^{\circ}$  N) enclosing the SMPDS data set, derived from the Climate Research Unit  
 905 CRU CL 2.0 database (New et al., 2002). The black points show climate values of the  
 906 SMPDS dataset. The red points show climate values of the Iberian Peninsula region in the  
 907 SMPDS dataset.  
 908



909

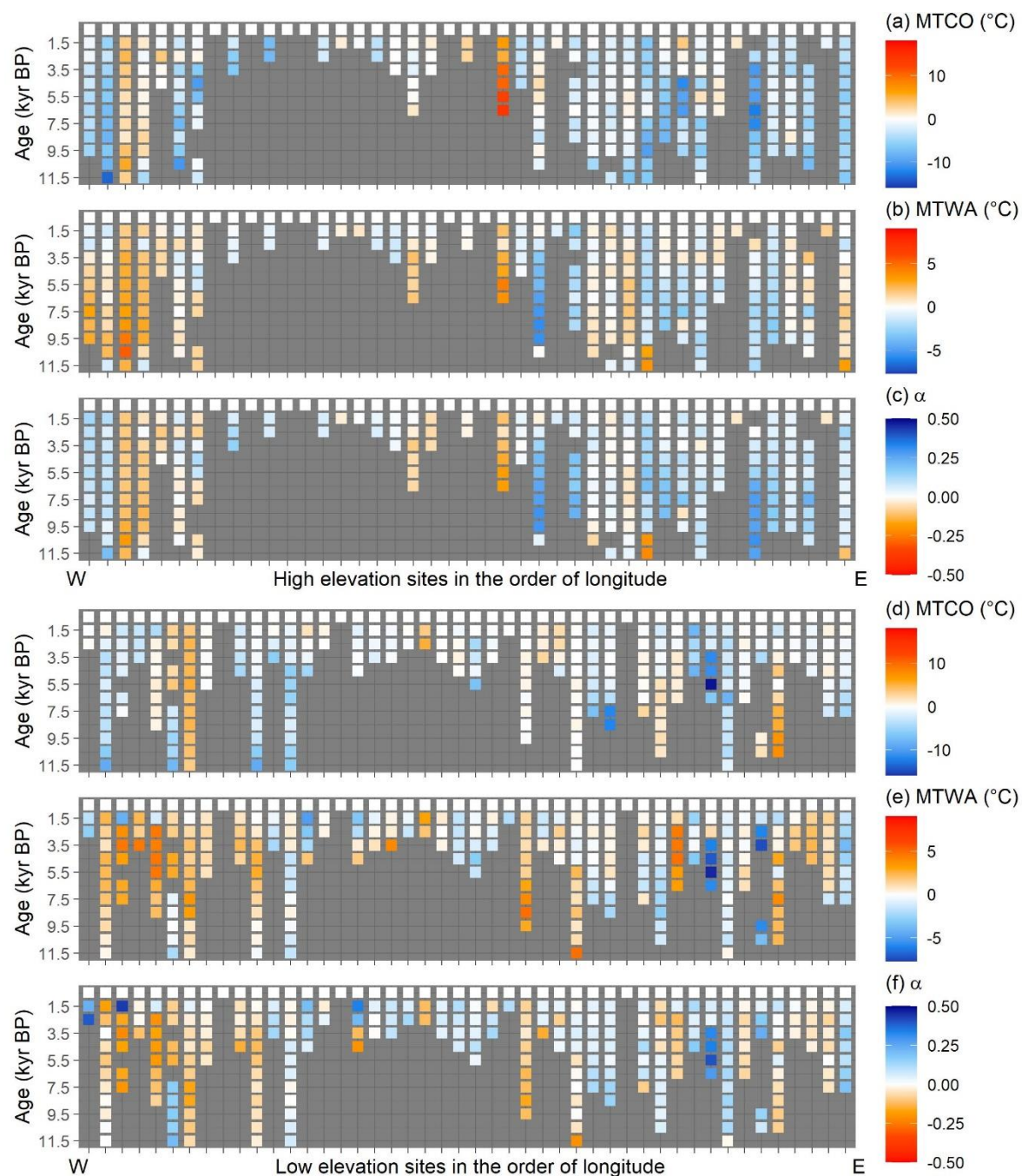
910 Figure 2. Map showing the location of the 117 fossil sites in the Iberian Peninsula used for  
 911 climate reconstructions. Sites lower than 1000 m a.s.l. are shown as squares, sites higher than  
 912 1000 m a.s.l. are shown as triangles. The base maps show modern (a) mean temperature of  
 913 the coldest month (MTCO), (b) mean temperature of the warmest month (MTWA), and (c)  
 914 plant-available moisture as represented by  $\alpha$ , an estimate of the ratio of actual  
 915 evapotranspiration to equilibrium evapotranspiration.

916



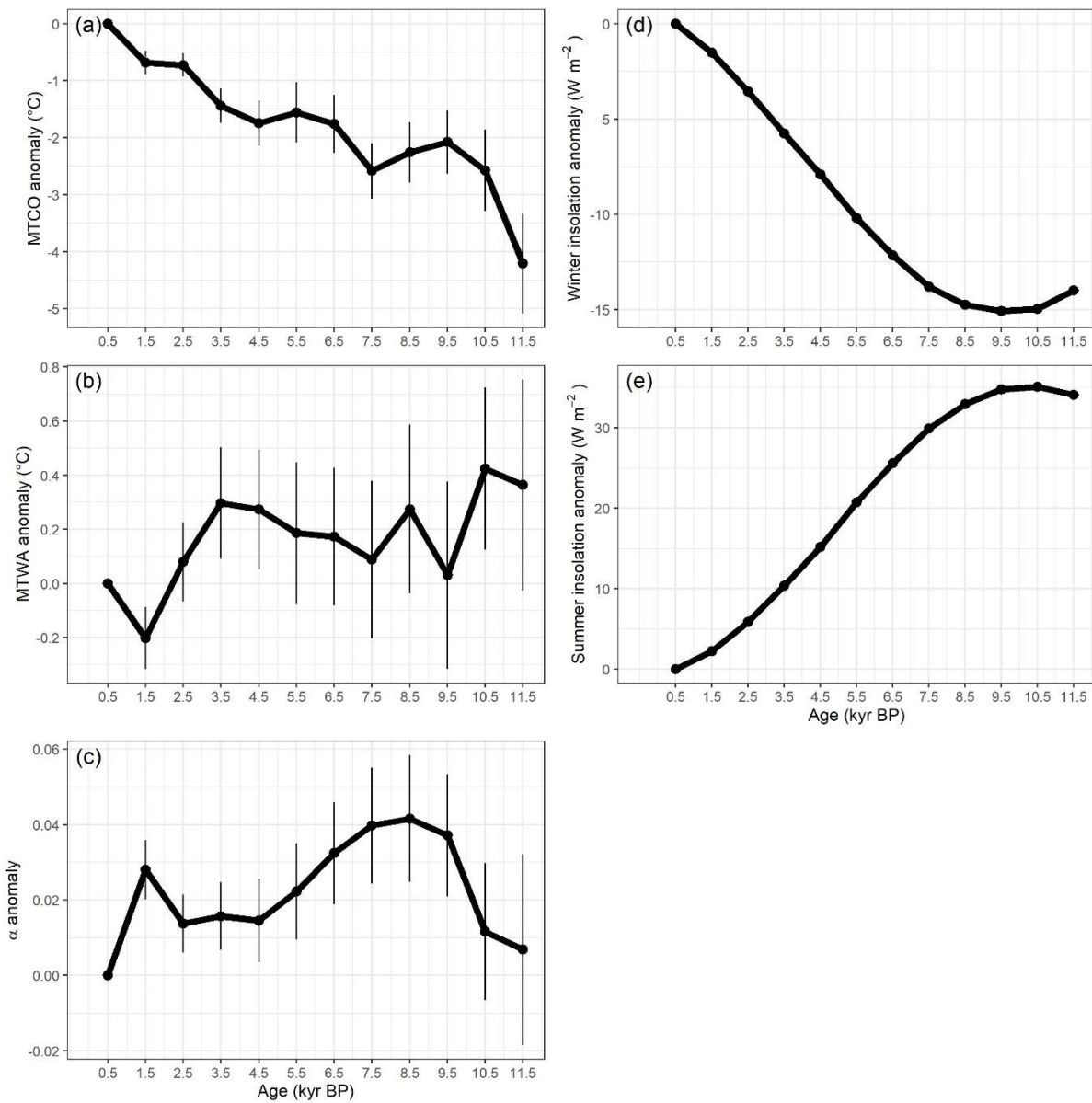
917

918 Figure 3. Reconstructed anomalies in climate at individual sites through time. The sites are  
 919 grouped into high (>1000m) and low (<1000m) elevation sites and organised from west to  
 920 east. Grey cells indicate periods or longitudes with no data. The individual plots show the  
 921 anomalies in reconstructed (a,d) mean temperature of the coldest month (MTCO), (b,e) mean  
 922 temperature of the warmest month (MTWA), and (c,f) plant-available moisture as  
 923 represented by  $\alpha$ , an estimate of the ratio of actual evapotranspiration to equilibrium  
 924 evapotranspiration. The anomalies are expressed as deviations of the mean value in each bin  
 925 ( $\pm 500$  years) from the value at 0.5 ka at each site.  
 926



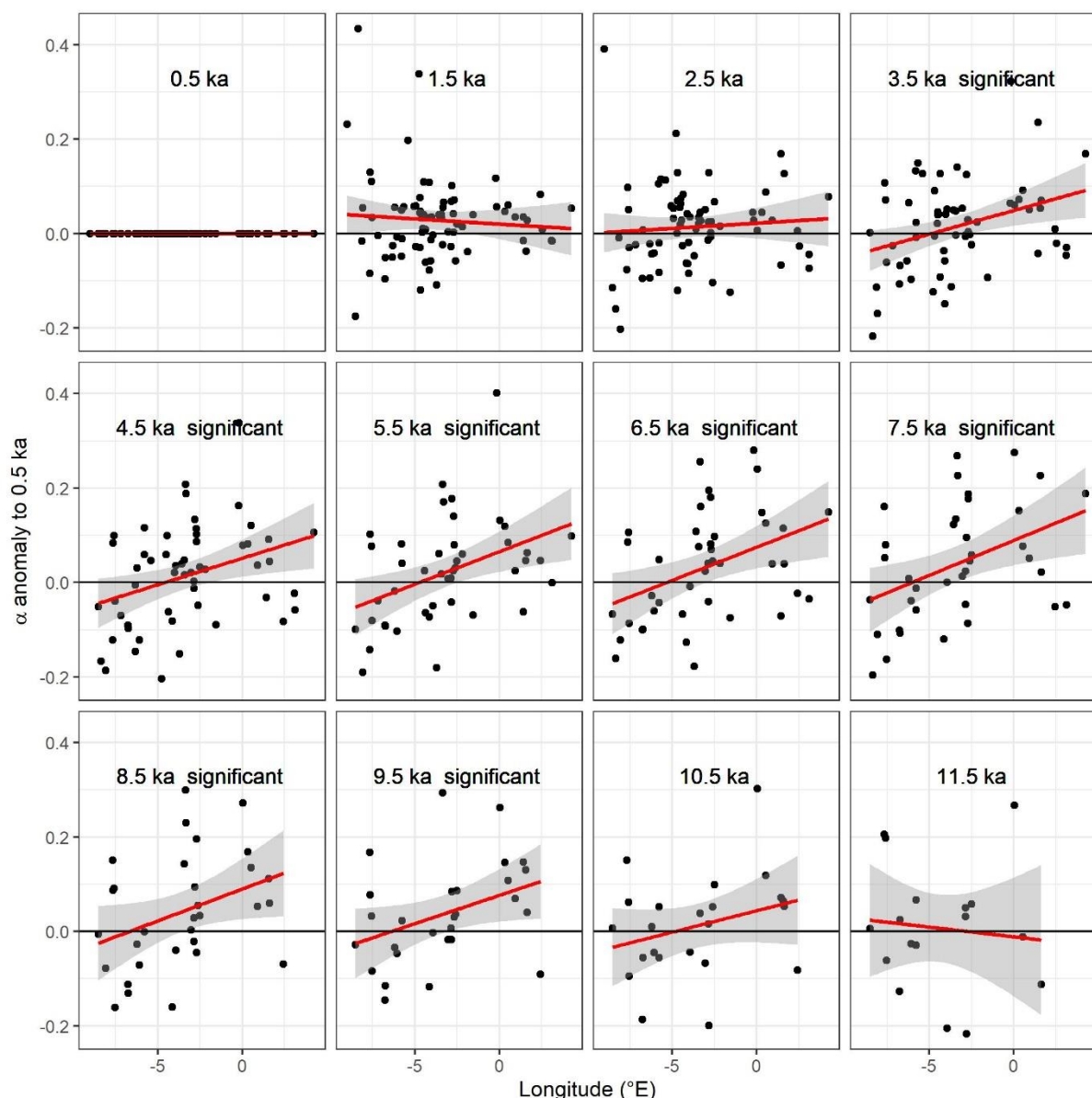
927

928 Figure 4. Reconstructed composite changes (anomalies to 0.5 ka) in (a) mean temperature of  
 929 the coldest month (MTCO), (b) mean temperature of the warmest month (MTWA) and (c)  
 930 plant-available moisture as represented by  $\alpha$ , through the Holocene compared to changes in  
 931 (d) winter and (e) summer insolation for the latitude of the Iberian Peninsula, using  $\pm 500$   
 932 years as the bin. The black lines show mean values across sites, with vertical line segments  
 933 showing the standard deviations of mean values using 1000 bootstrap cycles of site  
 934 resampling.  
 935



936

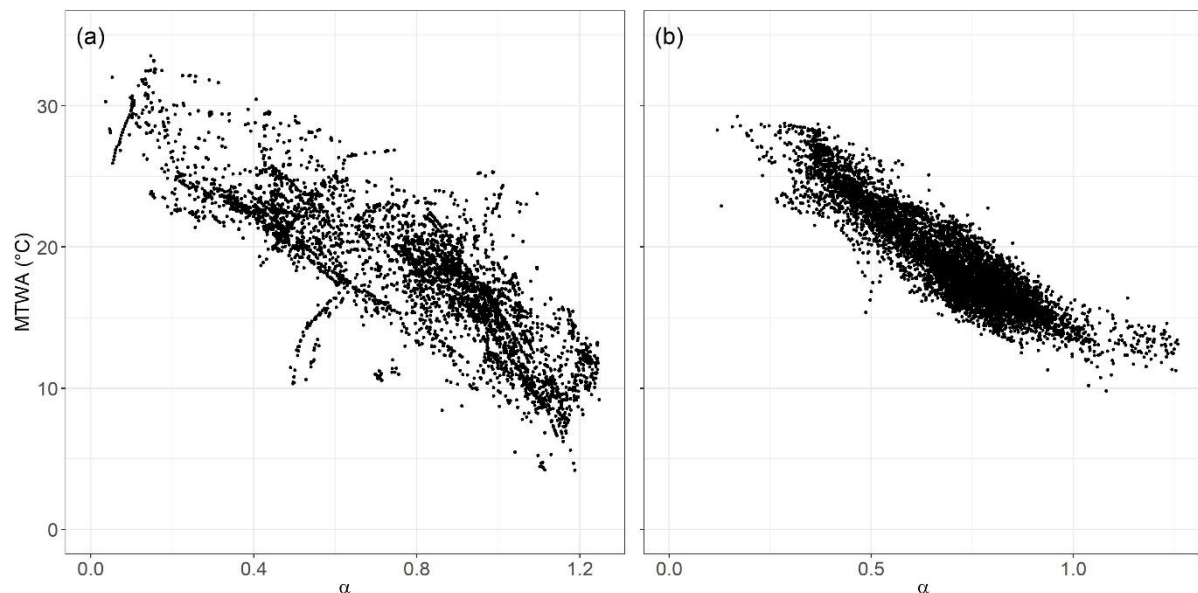
937 Figure 5. Changes in the west-east gradient of plant-available moisture as represented by  
 938 anomalies in  $\alpha$  relative to 0.5 ka at individual sites through the Holocene. The red lines show  
 939 the regression lines. The shades indicate the 95 % confidence intervals of the regression lines.  
 940



941

942 Figure 6. The relationship between mean temperature of the warmest month (MTWA) and  
943 plant-available moisture as represented by  $\alpha$  (a) in the modern climate data set, and (b) in the  
944 Holocene reconstructions.

945

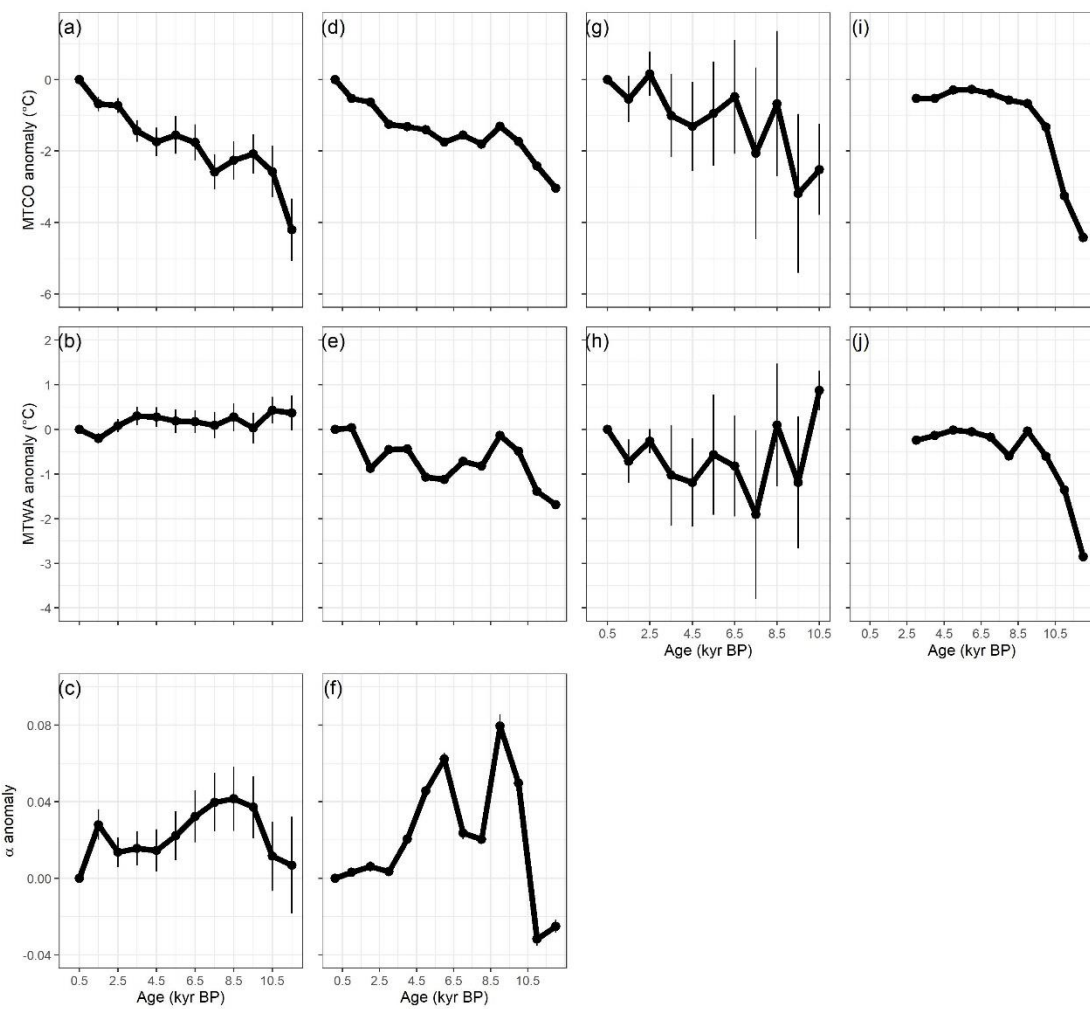


946

947

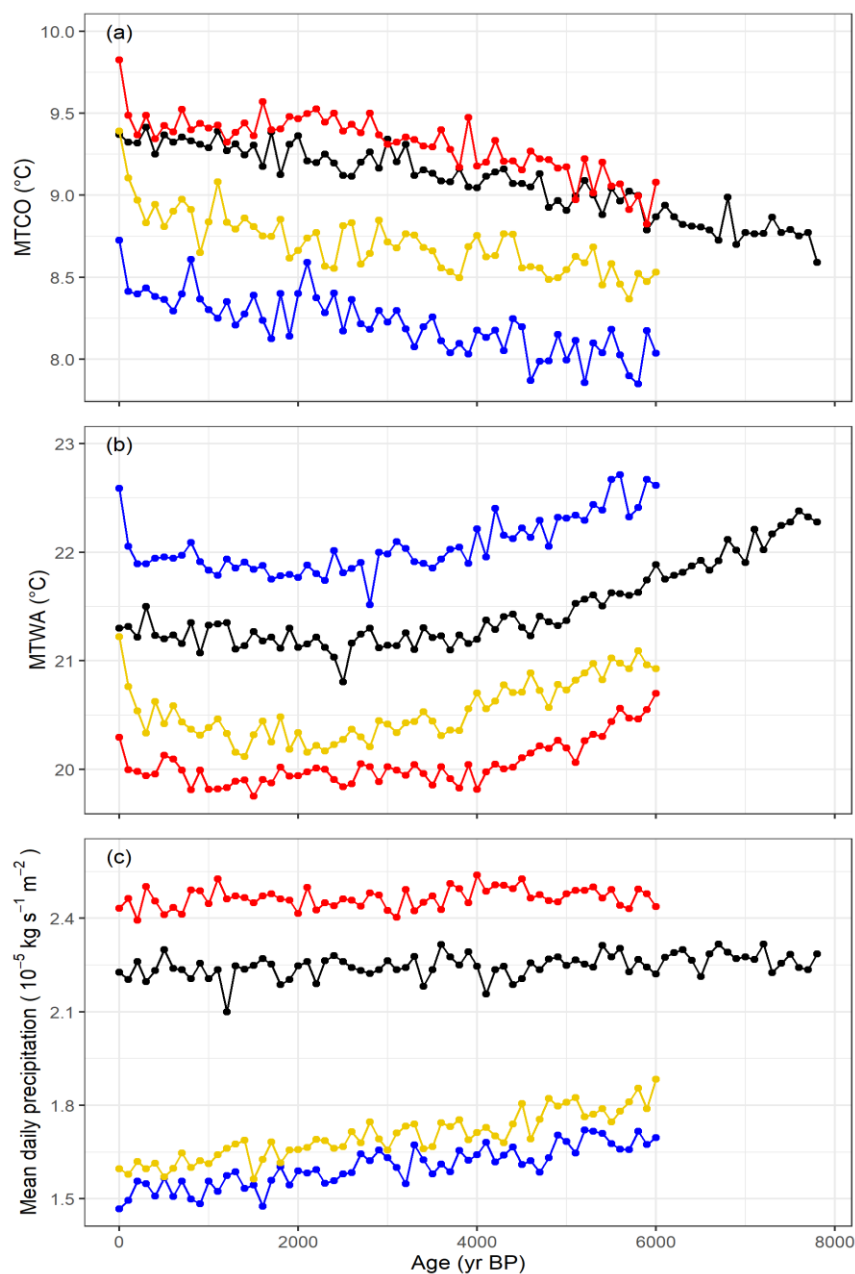
948

949 Figure 7. Comparison between reconstructed composite changes in climate anomalies. The first  
 950 column represents this paper, the second column represents Mauri et al. (2015), the third  
 951 column represents Kaufman et al. (2020), the fourth column represents Tarroso et al. (2016).  
 952 The composite curves from this paper and Kaufman et al. (2020) are calculated from individual  
 953 reconstructions, using anomalies to 0.5 ka and a bin of  $\pm 500$  years (time slices are 0.5, 1.5, ...,  
 954 11.5 ka). The composite curves from Mauri et al. (2015) are converted directly from the gridded  
 955 time slices which are provided with anomalies to 0.1 ka and a bin of  $\pm 500$  years (time slices  
 956 are 1, 2, ..., 12 ka). The composite curves from Tarroso et al. (2016) are also converted directly  
 957 from the gridded time slices provided, with anomalies to 0.5 ka and a bin of  $\pm 500$  years (time  
 958 slices are 3, 4, ..., 12 ka). Note that Tarroso et al. (2016) applied a smoothing to the data such  
 959 that the plots in the paper do not show the excursion in MTWA at 8 ka. In all of the plots, the  
 960 black lines show mean values across sites, with vertical line bars showing the standard  
 961 deviation of mean values using 1000 bootstrap cycles of site/grid resampling.  
 962



963  
 964

965 Figure 8. Simulated mean values of mean temperature of the coldest month (MTCO), mean  
 966 temperature of the warmest month (MTWA) and mean daily precipitation in Iberian  
 967 Peninsula between 8 ka and 0 ka, smoothed using 100 year bins. Here BP means before 1950  
 968 AD. The black lines represent Max Planck Institute Earth System Model (MPI) simulations,  
 969 the red lines represent Alfred Wagner Institute Earth System Model (AWI) simulations, the  
 970 blue lines represent Institut Pierre Simon Laplace Climate Model (IPSL-CM5) TR5AS  
 971 simulations, the orange lines represent Institut Pierre Simon Laplace Climate Model (IPSL-  
 972 CM6) TR6AV simulations. The four simulations were forced by evolving orbital parameters  
 973 and greenhouse gas concentrations. The four models have different spatial resolution, with  
 974 the finest resolution being  $1.875^\circ \times 1.875^\circ$  (AWI, MPI) and the coarsest resolution being  
 975  $1.875^\circ \times 3.75^\circ$  (IPSL-CM5, TR5AS).



976

977 Table 1. Details of the fossil pollen sites used. The fossil pollen data from the Iberian Peninsula were compiled by Shen et al. (2021) and obtained  
 978 from <https://doi.org/10.17864/1947.000343>. The reference list of this table can be found in the supplementary.  
 979

site name	entity name	longitude (°E)	latitude (°N)	elevation (m)	earliest sample (yr BP)	latest sample (yr BP)	length of record (yr)	no of samples	no of dating points	source	reference
Albufera Alcudia	ALCUDIA	3.12	39.79	0	7921	17	7904	54	4	EPD	Burjachs et al., (1994)
Algendar	ALGENDAR	3.96	39.94	21	8908	3816	5092	118	4	EPD	Yll et al., (1995, 1997)
Almenara de Adaja	ADAJA	-4.67	41.19	784	2830	477	2353	25	2	EPD	López Merino et al., (2009)
Alsa	ALSA	-4.02	43.12	560	4908	150	4758	24	3	EPD	Mariscal (1993)
Alvor Estuary Ribeira do Farelo Ribeira da Torre	Abi 05/07	-8.59	37.15	1	7840	1699	6141	76	9	author	Schneider et al., (2010, 2016)
Antas	ANTAS	-1.82	37.21	0	11141	4309	6832	95	6	EPD	Yll et al., (1995); Cano Villanueva, J. P. (1997); Pantaléon-Cano et al., (2003)
Arbarrain Mire	ARBARRAIN	-2.17	43.21	1004	6872	78	6794	91	8	author	Pérez-Díaz et al., (2018)
Armacao de Pera Ribeira de Alcantarilha	ADP 01/06	-8.34	37.11	2	7926	8	7918	17	7	author	Schneider et al., (2010, 2016)
Armena	Armena	0.34	42.51	2238	5668	2217	3451	53	27	author	Leunda et al., (2019)
Arroyo de Aguas Frias	AGUASFRIAS	-5.12	40.27	1120	196	-41	237	50	5	author	Julio Camarero et al., (2019)
Arroyo de las Cárcavas	CARCAVAS	-4.03	40.84	1300	2346	-57	2403	40	6	EPD	Morales-Molino et al., (2017a)
Arroyo de Navalacarreta	NAVALACA	-4.03	40.85	1250	706	-60	766	38	6	EPD	Morales-Molino et al., (2017a)
Arroyo de Valdeconejos	VALDECON	-4.06	40.86	1380	611	-56	667	44	8	EPD	Morales-Molino et al., (2017a)
Atxuri	ATXURI01	-1.55	43.25	500	6877	495	6382	33	2	EPD	Penalba (1994); Penalba and Garmendia (1989)
Ayoó de Vidriales	AYOO	-6.07	42.13	780	11846	-26	11872	63	15	EPD	Morales-Molino & García-Antón (2014)
Basa de la Mora	BSM08	0.33	42.55	1906	9856	184	9672	135	16	author	Pérez-Sanz et al., (2013)
Bassa Nera	BSN6	0.92	42.64	1891	9599	-55	9654	62	8	author	Garcés-Pastor et al., (2017)
Bermu Mire	BERMU	-4.15	39.43	783	1192	-25	1217	38	8	author	Luelmo-Lautenschlaeger et al., (2018a)
Borreguil de la Caldera	BdIC-01	-3.32	37.05	2992	1440	-56	1496	80	6	author	Ramos-Román et al., (2016)

Bosc dels Estanyons	BOSCESTA	1.63	42.48	2180	11761	26	11735	91	8	EPD	Miras et al., (2007); De Beaulieu et al., (2005)
Botija Bog	BOTIJA	-4.7	39.6	755	3773	82	3691	25	4	author	Luelmo-Lautenschlaeger et al., (2018b)
Cañada de la Cruz	CANCRUZ	-2.69	38.07	1595	9413	-6	9419	39	14	EPD	Yll et al., (1997)
Cala'n Porter	CPORTER	4.13	39.87	24	8809	4802	4007	86	4	EPD	Yll et al., (1994, 1995)
Cala Galdana	GALDANA	3.96	39.94	47	8498	4830	3668	101	5	EPD	López-Merino et al., (2012)
Campo Lameiro	PRD4	-8.52	42.53	260	11948	-11	11959	42	6	EPD	Carrión et al., (2007)
Canada del Gitano_Sierra de Baza	SBAZA	-2.7	37.23	1900	8460	103	8357	111	8	EPD	Cerrillo Cuenca et al., (2007); Cerrillo Cuenca & González Cordero (2011)
Canaleja	CANALEJA	-2.45	40.9	1029	11544	5515	6029	6	2	EPD	Carrión et al., (2001)
Castello Lagoon	Castello Lagoon core EM	3.1	42.28	2	4944	307	4637	85	10	author	Ejarque et al., (2016)
Cha das Lameiras	LAMEIRAS	-7.68	40.94	950	11982	539	11443	32	8	author	Burjachs & Expósito (2015)
Charco da Candieira	CANDIEIR	-7.58	40.34	1409	11970	32	11938	230	31	EPD	Mariscal Alvarez et al., (1983)
Creixell	CreixellT	1.43	41.16	1	6438	723	5715	32	2	EPD	López-Sáez et al., (2013)
Cueto de la Avellanosa	CUETOAV	-4.36	43.12	1320	6969	292	6677	34	3	EPD	López-Sáez et al., (2017)
Culazón	CULAZON	-4.49	43.23	592	3895	-44	3939	69	11	EPD	van der Knaap & van Leeuwen (1984, 1995, 1997)
El Brezosa	BREZOSA	-4.36	39.35	733	3958	-16	3974	68	11	author	Burjachs & Expósito (2015); Burjachs et al., (1997)
El Carrizal	CARRIZAL	-4.14	41.32	860	9851	0	9851	50	6	EPD	Morales-Molino et al., (2018)
El Maíllo mire	MAI	-6.21	40.55	1100	10687	91	10596	104	10	EPD	Franco-Múgica, et al., (2005)
El Payo	ELPAYO	-6.77	40.25	1000	571	-56	627	50	6	EPD	Morales-Molino et al., (2013)
El Perro mire	ELPERRO	-4.76	39.05	690	4694	-69	4763	41	10	author	Abel Schaad et al., (2009); Silva-Sánchez et al., (2016)
El Portalet	PORTALET	-0.4	42.8	1802	11838	2128	9710	207	13	author	Luelmo-Lautenschlaeger (2019a, 2019b)
El Redondo	REDONDO	-5.66	40.22	1765	3222	31	3191	60	4	author	González-Sampériz et al., (2006)
El Sabinar	SABINAR	-2.12	38.2	1117	6580	1140	5440	129	9	EPD	López-Sáez et al., (2016)
El Tiemblo	TIEMBLO	-4.53	40.36	1250	3184	3	3181	60	9	author	Carrión et al., (2004)
Elx	ELX	-0.75	38.17	1	9903	3392	6511	79	4	EPD	López-Sáez et al., (2018a)

Enol	ENOL	-4.99	43.27	1075	10910	2487	8423	30	7	author	Moreno et al., (2011)
Es Grau	ESGRAU	4.26	39.95	2	7648	-13	7661	98	15	EPD	Burjachs et al., (2017)
Espinosa de Cerrato	CERRATO	-3.94	41.96	885	11578	822	10756	157	7	author	Múgica et al., (2001); Morales-Molino et al., (2017b)
Estanilles	ESTANILLES	1.3	42.63	2247	11908	7646	4262	57	11	EPD	Pérez-Obiol et al., (2012)
Estanya	Estanya Catena	0.53	42.03	677	11882	-37	11919	48	21	author	González-Sampériz et al., (2017); Morellón et al., (2011)
Fuente de la Leche	LECHE	-5.06	40.35	1382	2783	-18	2801	58	10	author	Robles-López et al., (2018)
Fuente del Pino Blanco	PINOBLANCO	-4.98	40.24	1343	653	-38	691	96	5	author	Robles-López et al., (2018)
Hinojos Marsh	HINOJOS	-6.39	36.96	2	4737	2682	2055	46	5	author	López-Sáez et al., (2018b)
Hort Timoner	HTIMONER	4.13	39.88	40	8686	5089	3597	46	4	EPD	Yll et al., (1997)
Hoya del Castillo	N-CAS	-0.16	41.48	258	10740	5629	5111	34	3	EPD	Davis & Stevenson (2007)
La Cruz	LACRUZ	-1.87	39.99	1024	1521	12	1509	23	2	EPD	Burjachs (1996)
La Molina mire	MOLINAES	-6.33	43.38	650	4482	388	4094	152	6	author	López-Merino et al., (2011)
Labradillos Mire	LABRADILLOS	-4.57	40.34	1460	1447	184	1263	25	5	author	Robles López et al., (2017)
Lago de Ajo	LAGOAJO	-6.15	43.05	1570	11755	2175	9580	44	6	EPD	McKeever et al., (1984); Allen et al., (1996)
Lagoa Comprida 2	LAGOA_CO	-7.64	40.36	1650	9863	94	9769	68	4	EPD	Janssen & Woldringh (1981); Moe & Van Der Knaap (1990); Van Den Brink & Janssen (1985)
Lagoa Travessa	TRAVESS1	-8.77	38.3	3	8174	3617	4557	65	4	EPD	Mateus (1985); Mateus (1989)
Laguna de la Mosca	LdIMo composite	-3.31	37.06	2889	8344	-63	8407	68	18	author	Manzano et al., (2019)
Laguna de la Mula	LdIM 10-02	-3.42	37.06	2497	4581	-60	4641	32	8	author	Jiménez-Moreno et al., (2013)
Laguna de la Roya	LAROYA	-6.77	42.22	1608	11927	-41	11968	54	7	PANGAE A	Allen et al., (1996)
Laguna de Rio Seco	Laguna de Rio Seco core 1	-3.35	37.05	3020	10455	-54	10509	69	13	author	Anderson et al., (2011)
Laguna Guallar	N-GUA	-0.23	41.41	336	10654	8056	2598	30	6	EPD	Davis & Stevenson (2007)
Laguna Mesagosa	LAGMESAG	-2.81	41.97	1600	11981	-48	12029	90	5	EPD	Engelbrechten (1999)
Laguna Negra	LAGNEGRA	-2.85	42	1760	11253	-48	11301	68	9	EPD	Engelbrechten (1999)
Laguna Salada Chiprana	N-SAL	-0.17	41.23	150	6872	-40	6912	39	4	EPD	Valero-Garcés et al., (2000)

Lake Banyoles	BANYOLES_1, Banyoles SB2	2.75	42.13	174	11952	3316	8636	141	15	EPD	Pèrez-Obiol & Julià (1994); Revelles et al., (2015)
Lake Saloio	SALOIO	-9.02	39.61	70	2804	313	2491	24	2	EPD	Gomes (2011)
Lanzahíta	LANZBOG	-4.94	40.22	558	2657	-51	2708	51	8	author	López-Sáez et al., (1999, 2010)
Las Animas Mire	ANIMAS	-5.03	36.69	1403	797	-57	854	48	10	author	Alba-Sánchez et al., (2019)
Las Lanchas	LANCHAS	-4.89	39.59	800	374	-8	382	20	2	author	Luelmo-Lautenschlaeger et al., (2018c)
Las Pardillas	LASPARDI	-3.03	42.03	1850	10954	404	10550	74	4	EPD	Goñi & Hannon (1999)
Las Vinuelas	VINUELAS	-4.49	39.37	761	4210	-56	4266	58	9	author	Morales-Molino et al., (2019)
Les Palanques	PALANQUES	2.44	42.16	460	10011	524	9487	77	3	EPD	Revelles et al., (2018)
Manaderos	Manaderos core	-4.69	40.34	1292	1293	37	1256	59	9	author	Robles-López et al., (2020)
Marbore	Marbore composite	0.04	42.7	2612	11683	-18	11701	61	18	author	Leunda et al., (2017)
Monte Areo mire	AREO	-5.77	43.53	200	11547	-35	11582	55	12	EPD	López-Merino et al., (2010)
Montes do Buio Cuadramón	CUAII	-7.53	43.47	700	11347	241	11106	19	4	EPD	González et al., (2000)
Navamuno	Navamuno_S3	-5.78	40.32	1505	11971	-28	11999	207	12	author	López-Sáez et al., (2020)
Navarrés	NAVA1, NAVARRE3	-0.68	39.1	225	11104	3131	7973	72	15	EPD	Carrion & Dupre (1996); Carrión & Van Geel (1999)
Ojos del Tremendal	Ojos del Tremendal core 1	-2.04	40.54	1650	11875	1253	10622	52	4	author	Stevenson (2000)
Patateros bog	PATATERO	-4.67	39.6	700	2655	-19	2674	28	4	EPD	Dorado-Valiño et al., (2014)
Peña Negra	PENANEGR	-5.79	40.33	1000	3434	-62	3496	63	7	EPD	Stefanini (2008)
Pedrido	PEDRIDO	-7.07	43.44	770	5256	106	5150	71	30	EPD	Mighall et al., (2006)
Pena de Cadela	CADELA	-7.17	42.83	970	5233	-14	5247	91	9	EPD	Abel-Schaad & López-Sáez (2013)
Pico del Sertal	SERTAL	-4.44	43.22	940	5200	106	5094	9	3	EPD	Mariscal Alvarez (1986)
Pla de l'Estany	PLAESTANY	2.54	42.19	520	3577	-37	3614	43	4	EPD	Burjachs (1994)
Planell de Perafita	PERAFITA	1.57	42.48	2240	10244	-1	10245	56	11	EPD	Miras et al., (2010)
Posidonia Lligat	LLIGAT	-3.29	42.29	-3	779	15	764	32	5	EPD	López-Sáez et al., (2009)
Pozo de la Nieve	PozoN_2015 core	-4.55	40.35	1600	2258	-37	2295	41	10	author	Robles-López et al., (2017)

Prailllos de Bossier Mire	BOSSIER	-4.07	36.91	1610	3428	4	3424	25	3	EPD	Abel-Schaad et al., (2017)
Prat de Vila	PRATVILA	1.43	38.92	4	10776	538	10238	29	5	EPD	Burjachs et al., (2017)
Puerto de Belate	BELATE01	-2.05	43.03	847	8457	1746	6711	60	3	EPD	Penalba (1994); Penalba and Garmendia (1989)
Puerto de las Estaces de Trueba	ESTACAS	-3.7	43.12	1160	6263	391	5872	9	3	PANGAE A	Mariscal (1989)
Puerto de Los Tornos	TORNOS01	-3.43	43.15	920	8718	-34	8752	47	4	EPD	Penalba and Garmendia (1989)
Puerto de Serranillos	SERRANIL	-4.93	40.31	1700	2254	-50	2304	34	5	EPD	López-Merino et al., (2009)
Quintanar de la Sierra	QUINTA02	-3.02	42.03	1470	11995	1953	10042	37	20	EPD	Penalba (1994); Penalba and Garmendia (1989)
Roquetas de Mar	ROQUETAS	-2.59	36.79	0	6910	1057	5853	32	3	EPD	Yll et al., (1995); Cano Villanueva (1997); Pantaléon-Cano (2003); Obiol (1994)
Salada Pequeña	N-PEQ	-0.22	41.03	357	4350	669	3681	43	5	EPD	Davis (2010)
Saldropo	SALDROPO	-2.72	43.05	625	7577	403	7174	76	3	EPD	Penalba (1994, 1989)
Salines playa-lake	SALINES	-0.89	38.5	475	11905	1394	10511	74	7	EPD	Burjachs et al., (2017)
San Rafael	SANRAFA	-2.6	36.77	0	10846	-30	10876	134	6	EPD	Cano Villanueva (1997); Pantaléon-Cano et al., (2003); Yll et al., (1995)
Sanabria Marsh	SANABRIA	-6.73	42.1	1050	11832	0	11832	79	9	EPD	Allen et al., (1996); Hannon (1985); Turner & Hannon (1988)
Serra Mitjana Fen	MITJANA	1.58	42.47	2406	1490	412	1078	15	2	EPD	Miras et al., (2015)
Serranía de las Villuercas	VILLUERCAS	-5.4	39.48	1000	4156	128	4028	31	4	author	Gil-Romera et al., (2008)
Sierra de Gádor	GADOR	-2.92	36.9	1530	6222	1195	5027	86	6	EPD	Carrión et al., (2003)
Siles Lake	SILES	-2.5	38.4	1320	11527	189	11338	67	12	EPD	Carrión (2002)
Tubilla del Lago	TUB	-3.57	41.81	900	7436	31	7405	88	13	EPD	Morales-Molino et al., (2017b)
Turbera de La Panera Cabras	PANERA	-5.76	40.17	1648	164	-56	220	23	2	EPD	Abel Schaad et al., (2009)
Valdeyernos bog	VALDEYER	-4.1	39.44	850	3160	-60	3220	25	4	EPD	Dorado-Valiño et al., (2014)
Valle do Lobo Ribeira de Carcavai	VdL PB2	-8.07	37.06	2	8331	16	8315	144	20	author	Schneider et al., (2010, 2016)
Verdeospesoa mire	VERDEOSPES OA	-2.86	43.06	1015	11137	0	11137	91	12	author	Pérez-Díaz & López-Sáez (2017)

Vilamora Ribeira de Quarteira	Vilamora P01-5	-8.14	37.09	4	3851	919	2932	30	12	author	Schneider et al., (2010, 2016)
Villaverde	VILLAVERDE	-2.37	38.8	870	8066	0	8066	104	9	EPD	Carrión et al., (2001)
Xan de Llamas	XL	-6.32	42.3	1500	4113	34	4079	33	4	EPD	Morales-Molino et al., (2011)
Zoñar	ZONARcombi ned	-4.69	37.48	300	3234	-45	3279	52	17	author	Martín-Puertas et al., (2008)

980

981 Table 2. Leave-out cross-validation (with geographically and climatically close sites  
 982 removed) fitness of the modified version of fxtWA-PLS, for mean temperature of the coldest  
 983 month (MTCO), mean temperature of the warmest month (MTWA) and plant-available  
 984 moisture ( $\alpha$ ), with p-spline smoothed fx estimation, using bins of 0.02, 0.02 and 0.002,  
 985 showing results for all the components. RMSEP is the root-mean-square error of prediction.  
 986  $\Delta$ RMSEP is the per cent change of RMSEP using the current number of components than  
 987 using one component less.  $p$  assesses whether using the current number of components is  
 988 significantly different from using one component less, which is used to choose the last  
 989 significant number of components (indicated in bold) to avoid over-fitting. The degree of  
 990 overall compression is assessed by linear regression of the cross-validated reconstructions  
 991 onto the climate variable,  $b_1$ ,  $b_1$ .se are the slope and the standard error of the slope,  
 992 respectively. The closer the slope ( $b_1$ ) is to 1, the less the overall compression is.  
 993  
 994

	ncomp	$R^2$	avg. bias	max. bias	min. bias	RMSEP	$\Delta$ RMSEP	$p$	$b_1$	$b_1$ .se
MTCO	1	0.70	-0.86	25.23	0.00	5.20	-39.97	0.001	0.89	0.01
	2	0.73	-0.73	25.00	0.00	4.87	-6.29	0.001	0.91	0.01
	3	0.74	-0.71	24.38	0.00	4.86	-0.32	0.001	0.91	0.01
	<b>4</b>	<b>0.75</b>	<b>-0.59</b>	<b>24.27</b>	<b>0.00</b>	<b>4.70</b>	<b>-3.26</b>	<b>0.001</b>	<b>0.91</b>	<b>0.01</b>
	5	0.74	-0.63	34.54	0.00	4.77	1.51	1.000	0.91	0.01
MTWA	1	0.52	-0.29	17.13	0.00	3.72	-26.88	0.001	0.69	0.01
	2	0.56	-0.14	17.20	0.00	3.53	-5.06	0.001	0.71	0.01
	3	0.56	-0.13	17.01	0.00	3.53	-0.20	0.008	0.71	0.01
	<b>4</b>	<b>0.57</b>	<b>-0.11</b>	<b>17.30</b>	<b>0.00</b>	<b>3.47</b>	<b>-1.56</b>	<b>0.001</b>	<b>0.71</b>	<b>0.01</b>
	5	0.57	-0.11	17.34	0.00	3.48	0.10	0.780	0.71	0.01
$\alpha$	1	0.65	-0.014	0.787	0.000	0.165	-39.59	0.001	0.76	0.01
	2	0.68	-0.016	0.781	0.000	0.159	-3.55	0.001	0.77	0.01
	<b>3</b>	<b>0.68</b>	<b>-0.017</b>	<b>0.757</b>	<b>0.000</b>	<b>0.158</b>	<b>-0.61</b>	<b>0.023</b>	<b>0.78</b>	<b>0.01</b>
	4	0.69	-0.017	0.784	0.000	0.158	-0.43	0.108	0.79	0.01
	5	0.69	-0.017	0.850	0.000	0.158	0.26	0.985	0.80	0.01

995

996 Table 3. Canonical Correspondence Analysis (CCA) result of modern and fossil-  
 997 reconstructed MTCO, MTWA and  $\alpha$ . The summary statistics for the ANOVA-like  
 998 permutation test (999 permutations) are also shown. VIF is the variance inflation factor, Df is  
 999 the number of degrees of freedom,  $\chi^2$  is the constrained eigenvalue (or the sum of constrained  
 1000 eigenvalues for the whole model), F is significance, and Pr (>F) is the probability. The CCA  
 1001 plots can be found in the Supplementary (Fig. S11).  
 1002

	<b>Axes</b>	<b>Axis 1</b>	<b>Axis 2</b>	<b>Axis 3</b>	<b>VIF</b>
	Constrained eigenvalues	0.3819	0.1623	0.1087	/
<b>Correlations of the environmental variables with the axes:</b>					
	MTCO	-0.815	0.579	0.012	1.31
	MTWA	-0.700	-0.203	0.685	3.34
	$\alpha$	0.883	0.430	-0.187	3.39
	<b>Df</b>	<b><math>\chi^2</math></b>	<b>F</b>	<b>Pr (&gt;F)</b>	
Modern	Whole model	3	0.6530	78.113	0.001
	MTCO	1	0.3082	110.597	0.001
	MTWA	1	0.1602	57.489	0.001
	$\alpha$	1	0.1846	66.252	0.001
	CCA 1	1	0.3819	137.076	0.001
	CCA 2	1	0.1623	58.252	0.001
	CCA 3	1	0.1087	39.011	0.001
	<b>Axes</b>	<b>Axis 1</b>	<b>Axis 2</b>	<b>Axis 3</b>	<b>VIF</b>
Fossil-reconstructed	Constrained eigenvalues	0.3601	0.2266	0.2037	/
<b>Correlations of the environmental variables with the axes:</b>					
	MTCO	0.430	0.776	0.462	1.34
	MTWA	0.987	0.141	-0.076	5.40
	$\alpha$	-0.947	0.088	-0.308	5.28
	<b>Df</b>	<b><math>\chi^2</math></b>	<b>F</b>	<b>Pr (&gt;F)</b>	
	Whole model	3	0.7905	226.98	0.001
	MTCO	1	0.2465	212.34	0.001
	MTWA	1	0.3298	284.07	0.001
	$\alpha$	1	0.2142	184.53	0.001
	CCA 1	1	0.3601	310.19	0.001
	CCA 2	1	0.2266	195.24	0.001
	CCA 3	1	0.2037	175.51	0.001

1003

1004  
 1005 Table 4. Assessment of the significance of anomalies to 0.5 ka through time with latitude and  
 1006 elevation. The slope is obtained by linear regression of the anomaly onto the longitude or  
 1007 elevation.  $p$  is the significance of the slope (bold parts:  $p < 0.05$ ).  $x_0$  is the point where the  
 1008 anomaly is 0 in the linear equation, which indicates longitude or elevation where the anomaly  
 1009 changes sign.

		Longitude (°E)				Elevation (km)		
		age (ka)	slope	$p$	$x_0$	slope	$p$	$x_0$
MTCO (°C)	0.5	0.00	/	/	0.00	/	/	
	1.5	-0.07	0.411	-13.02	-0.30	0.411	-1.21	
	2.5	-0.15	0.095	-8.56	-0.52	0.179	-0.40	
	3.5	-0.13	0.314	-14.83	-0.81	0.142	-0.77	
	4.5	-0.12	0.444	-17.28	-0.69	0.319	-1.46	
	5.5	-0.24	0.247	-9.49	-0.61	0.503	-1.43	
	6.5	-0.18	0.372	-12.74	-0.87	0.293	-0.88	
	7.5	-0.15	0.421	-20.39	-1.38	0.080	-0.67	
	8.5	-0.03	0.890	-77.87	-1.58	0.065	-0.10	
	9.5	0.01	0.954	156.31	-1.79	0.060	0.11	
	10.5	0.20	0.474	9.25	-1.38	0.241	-0.64	
	11.5	0.23	0.528	13.77	0.12	0.947	36.35	
MTWA (°C)	0.5	0.00	/	/	0.00	/	/	
	1.5	-0.01	0.862	-26.38	-0.05	0.830	-3.35	
	2.5	-0.09	0.137	-2.80	-0.45	0.092	1.19	
	3.5	<b>-0.23</b>	<b>0.005</b>	<b>-2.03</b>	-0.40	0.284	1.74	
	4.5	<b>-0.21</b>	<b>0.016</b>	<b>-2.01</b>	-0.58	0.126	1.55	
	5.5	<b>-0.26</b>	<b>0.011</b>	<b>-2.43</b>	-0.49	0.280	1.53	
	6.5	<b>-0.24</b>	<b>0.017</b>	<b>-2.30</b>	-0.62	0.137	1.41	
	7.5	<b>-0.26</b>	<b>0.012</b>	<b>-3.02</b>	<b>-1.05</b>	<b>0.019</b>	<b>1.28</b>	
	8.5	-0.24	0.061	-2.43	<b>-1.15</b>	<b>0.023</b>	<b>1.57</b>	
	9.5	<b>-0.32</b>	<b>0.013</b>	<b>-3.20</b>	-0.44	0.459	1.34	
	10.5	-0.18	0.115	-1.23	0.54	0.276	0.44	
	11.5	0.13	0.453	-7.25	0.37	0.663	0.22	
$\alpha$	0.5	0.00	/	/	0.00	/	/	
	1.5	0.00	0.508	8.99	-0.01	0.393	3.40	
	2.5	0.00	0.517	-9.89	0.02	0.249	0.19	
	3.5	<b>0.01</b>	<b>0.006</b>	<b>-4.91</b>	0.02	0.191	0.28	
	4.5	<b>0.01</b>	<b>0.010</b>	<b>-4.60</b>	<b>0.05</b>	<b>0.008</b>	<b>0.79</b>	
	5.5	<b>0.01</b>	<b>0.005</b>	<b>-4.75</b>	<b>0.05</b>	<b>0.027</b>	<b>0.67</b>	
	6.5	<b>0.01</b>	<b>0.007</b>	<b>-5.34</b>	<b>0.06</b>	<b>0.004</b>	<b>0.60</b>	
	7.5	<b>0.02</b>	<b>0.009</b>	<b>-6.05</b>	<b>0.09</b>	<b>0.000</b>	<b>0.75</b>	
	8.5	<b>0.01</b>	<b>0.049</b>	<b>-6.67</b>	<b>0.09</b>	<b>0.000</b>	<b>0.88</b>	
	9.5	<b>0.01</b>	<b>0.048</b>	<b>-6.40</b>	<b>0.07</b>	<b>0.012</b>	<b>0.70</b>	
	10.5	0.01	0.183	-4.85	0.02	0.535	0.59	
	11.5	0.00	0.713	-2.76	0.03	0.654	0.93	

1011 **Appendix A**

1012 **Theoretical basis:**

1013 **The previous version of fxTWA-PLS (fxTWA-PLS1):**

1014 The estimated optimum ( $\hat{u}_k$ ) and unbiased tolerance ( $\hat{t}_k$ ) of each taxon are calculated from  
1015 the modern training data set as follows:

$$1016 \quad \hat{u}_k = \frac{\sum_{i=1}^n y_{ik} x_i}{\sum_{i=1}^n y_{ik}} \quad (A1)$$

$$1017 \quad \hat{t}_k = \sqrt{\frac{\sum_{i=1}^n y_{ik} (x_i - \hat{u}_k)^2}{(1 - 1/N_{2k}) \sum_{i=1}^n y_{ik}}} \quad (A2)$$

1018 where

$$1019 \quad N_{2k} = \frac{1}{\sum_{i=1}^n \left( \frac{y_{ik}}{\sum_{i'=1}^n y_{i'k}} \right)^2} \quad (A3)$$

1020 where  $n$  is the total number of sites;  $y_{ik}$  is the observed abundance of the  $k^{th}$  taxon at the  $i^{th}$   
1021 site;  $x_i$  is the observed climate value at the  $i^{th}$  site;  $N_{2k}$  is the effective number of occurrences  
1022 for the  $k^{th}$  taxon.

1023 fx correction is applied as weight in the form of  $1/fx^2$  at regression at step 7 in Table 1 in Liu  
1024 et al. (2020). The regression step uses robust linear model fitting by the R code:

$$1026 \quad rlm(x_i \sim comp_1 + comp_2 + \dots + comp_{pls}, weights = 1/fx^2) \quad (A4)$$

1027

1028 **The modified version of fxTWA-PLS (fxTWA-PLS2):**

1029 The distribution of  $y_{ik}$  is influenced by the distribution of the climate variable, so we need to  
1030 apply the fx correction when calculating optimum and tolerance for each taxon as follows:

$$1031 \quad \hat{u}_k = \frac{\sum_{i=1}^n \frac{y_{ik} x_i}{f_{x_i}}}{\sum_{i=1}^n \frac{y_{ik}}{f_{x_i}}} \quad (A5)$$

$$1032 \quad \hat{t}_k = \sqrt{\frac{\sum_{i=1}^n \frac{y_{ik} (x_i - \hat{u}_k)^2}{f_{x_i}}}{\left(1 - \frac{1}{N_{2k}}\right) \sum_{i=1}^n \frac{y_{ik}}{f_{x_i}}}} \quad (A6)$$

1033 where

$$1034 \quad N_{2k} = \frac{1}{\sum_{i=1}^n \left( \frac{\frac{y_{ik}}{f_{x_i}}}{\sum_{i'=1}^n \frac{y_{i'k}}{f_{x_{i'}}}} \right)^2} \quad (A7)$$

1035 The modified version of fxTWA-PLS applies fx correction separately at taxon calculation  
1036 and regression (step 2 and 7 in Table 1 in Liu et al., 2020), both using weight in the form of  
1037  $1/fx$ . The regression step (step 7) then becomes:

1038  $rlm(x_i \sim comp_1 + comp_2 + \dots + comp_{pls}, weights = 1/fx)$  (A8)

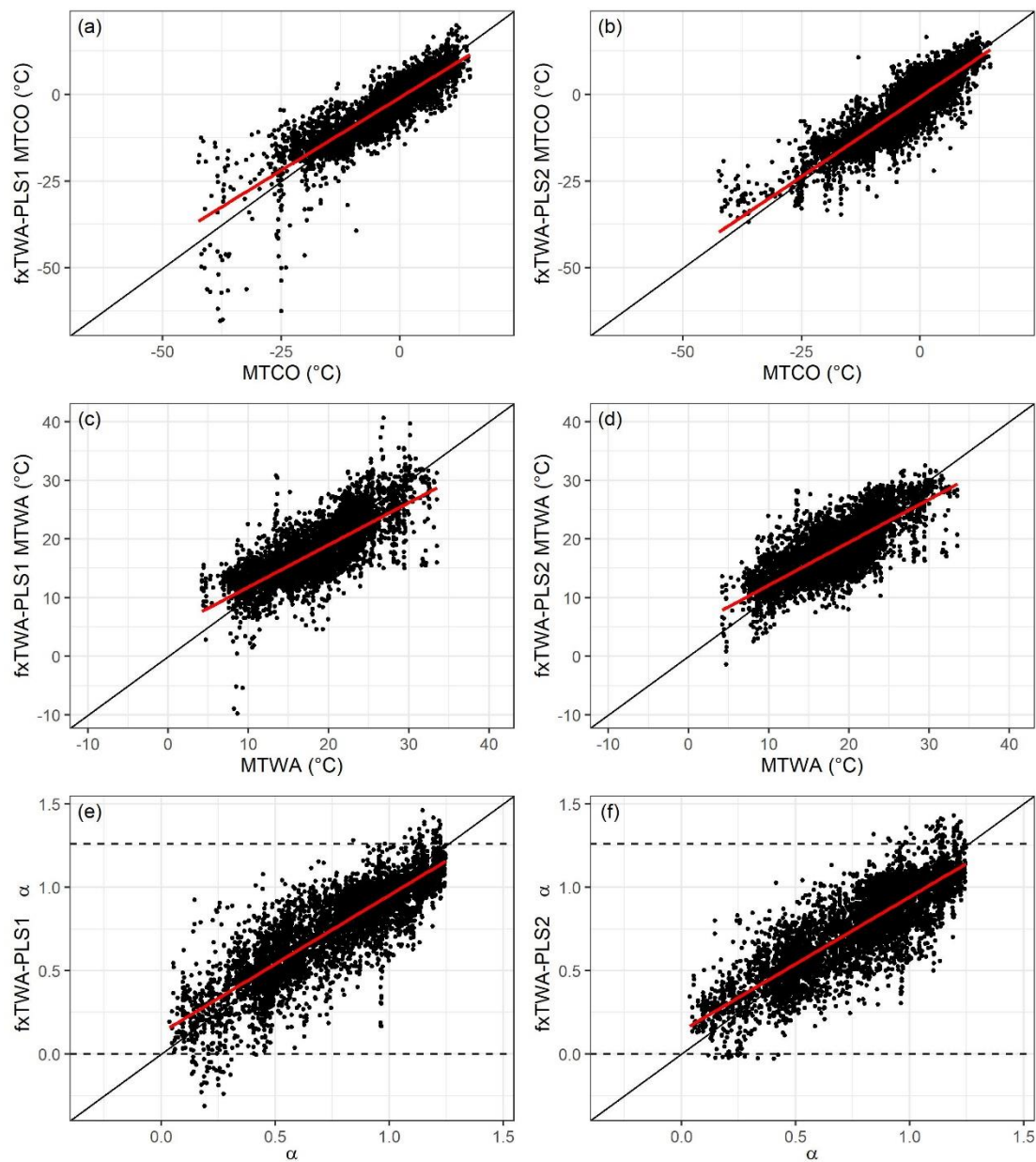
1039 The previous version uses fx values extracted from histograms, and different bin widths may  
1040 result in different training results. The modified version applies P-splines histogram  
1041 smoothing (Eilers and Marx, 2021) with third order difference penalty, which makes the fx  
1042 values almost independent on the bin width. The optimal smoothing parameter of the P-spline  
1043 penalty was determined by the HFS (Harville-Fellner-Schall) algorithm (Eilers and Marx,  
1044 2021) for the Poisson likelihood for the histogram counts.

1045 Table A1. Leave-out cross-validation (with geographically and climatically close sites removed)  
 1046 fitness of the previous and modified version of fxTWA-PLS (fxTWA-PLS1 and fxTWA-PLS2,  
 1047 respectively), for mean temperature of the coldest month (MTCO), mean temperature of the warmest  
 1048 month (MTWA) and plant-available moisture ( $\alpha$ ), using bins of 0.02, 0.02 and 0.002, respectively. n  
 1049 is the number of components used. RMSEP is the root mean square error of prediction.  $\Delta$ RMSEP is  
 1050 the per cent change of RMSEP using the current number of components than using one component  
 1051 less.  $p$  assesses whether using the current number of components is significantly different from using  
 1052 one component less, which is used to choose the last significant number of components (indicated in  
 1053 bold) to avoid overfitting. The degree of overall compression is assessed by doing linear regression to  
 1054 the cross-validation result and the climate variable. b1, b1.se are the slope and the standard error of  
 1055 the slope, respectively. The closer the slope (b1) is to 1, the lower the overall compression is. fx  
 1056 correction is set intrinsic in functions in fxTWAPLS package for both versions in this paper, instead  
 1057 of relying on an outside input in Liu et al. (2020), so the values of fxTWA-PLS1 might be slighted  
 1058 different from values in Table 3 in Liu et al. (2020), but it doesn't affect the conclusion.  
 1059

	Method	n	$R^2$	avg. bias	max. bias	min. bias	RMSEP	$\Delta$ RMSEP	$p$	b1	b1.se
MTCO	fxTWA-PLS1	1	0.66	-0.86	31.17	0.00	5.21	-39.87	0.001	0.76	0.01
		2	0.72	-0.52	36.65	0.00	4.70	-9.78	0.001	0.80	0.01
		3	0.73	-0.47	41.18	0.00	4.62	-1.63	0.001	0.82	0.01
		<b>4</b>	<b>0.73</b>	<b>-0.51</b>	<b>44.86</b>	<b>0.00</b>	<b>4.58</b>	<b>-1.01</b>	<b>0.006</b>	<b>0.82</b>	<b>0.01</b>
	fxTWA-PLS2	5	0.73	-0.41	58.35	0.00	4.62	0.89	0.708	0.83	0.01
		1	0.70	-0.86	25.23	0.00	5.20	-39.97	0.001	0.89	0.01
		2	0.73	-0.73	25.00	0.00	4.87	-6.29	0.001	0.91	0.01
		3	0.74	-0.71	24.38	0.00	4.86	-0.32	0.001	0.91	0.01
		<b>4</b>	<b>0.75</b>	<b>-0.59</b>	<b>24.27</b>	<b>0.00</b>	<b>4.70</b>	<b>-3.26</b>	<b>0.001</b>	<b>0.91</b>	<b>0.01</b>
		5	0.74	-0.63	34.54	0.00	4.77	1.51	1.000	0.91	0.01
MTWA	fxTWA-PLS1	1	0.50	-0.53	17.91	0.00	3.87	-24.09	0.001	0.67	0.01
		<b>2</b>	<b>0.56</b>	<b>-0.54</b>	<b>17.71</b>	<b>0.00</b>	<b>3.52</b>	<b>-8.98</b>	<b>0.001</b>	<b>0.69</b>	<b>0.01</b>
		3	0.57	-0.49	25.14	0.00	3.52	0.09	0.565	0.73	0.01
		4	0.57	-0.43	34.92	0.00	3.56	1.12	0.974	0.75	0.01
		5	0.57	-0.46	32.23	0.00	3.55	-0.23	0.139	0.74	0.01
	fxTWA-PLS2	1	0.52	-0.29	17.13	0.00	3.72	-26.88	0.001	0.69	0.01
		2	0.56	-0.14	17.20	0.00	3.53	-5.06	0.001	0.71	0.01
		3	0.56	-0.13	17.01	0.00	3.53	-0.20	0.008	0.71	0.01
		<b>4</b>	<b>0.57</b>	<b>-0.11</b>	<b>17.30</b>	<b>0.00</b>	<b>3.47</b>	<b>-1.56</b>	<b>0.001</b>	<b>0.71</b>	<b>0.01</b>
		5	0.57	-0.11	17.34	0.00	3.48	0.10	0.780	0.71	0.01
$\alpha$	fxTWA-PLS1	1	0.63	-0.020	0.773	0.000	0.174	-36.23	0.001	0.78	0.01
		2	0.69	-0.012	0.902	0.000	0.157	-9.66	0.001	0.79	0.01
		<b>3</b>	<b>0.69</b>	<b>-0.011</b>	<b>0.820</b>	<b>0.000</b>	<b>0.155</b>	<b>-1.28</b>	<b>0.001</b>	<b>0.79</b>	<b>0.01</b>
		4	0.70	-0.010	0.786	0.000	0.156	0.25	0.867	0.81	0.01
		5	0.70	-0.010	0.786	0.000	0.156	0.09	1.000	0.81	0.01
	fxTWA-PLS2	1	0.65	-0.014	0.787	0.000	0.165	-39.59	0.001	0.76	0.01
		2	0.68	-0.016	0.781	0.000	0.159	-3.55	0.001	0.77	0.01
		<b>3</b>	<b>0.68</b>	<b>-0.017</b>	<b>0.757</b>	<b>0.000</b>	<b>0.158</b>	<b>-0.61</b>	<b>0.023</b>	<b>0.78</b>	<b>0.01</b>
		4	0.69	-0.017	0.784	0.000	0.158	-0.43	0.108	0.79	0.01
		5	0.69	-0.017	0.850	0.000	0.158	0.26	0.985	0.80	0.01

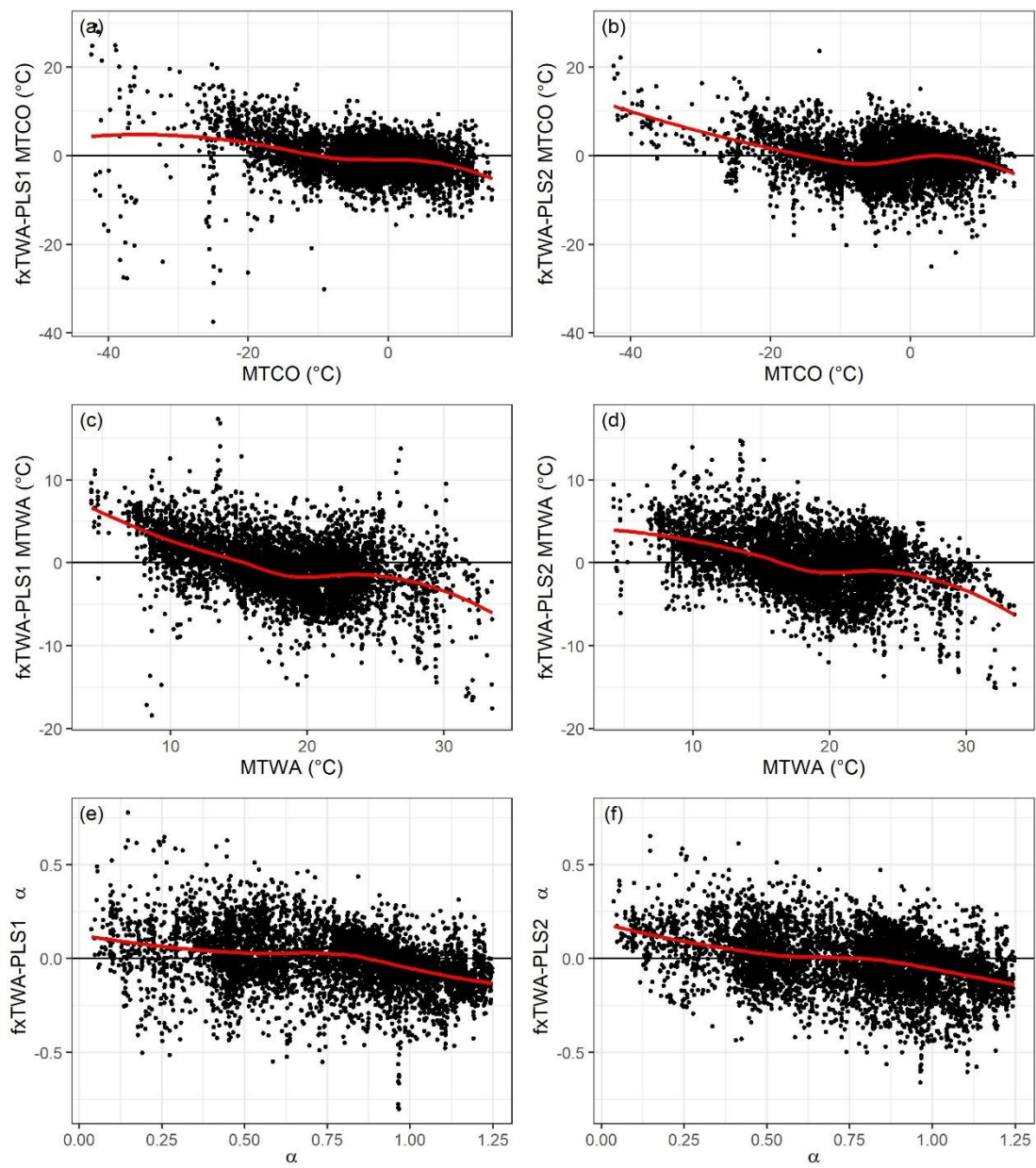
1060  
 1061

1062 Figure A1. Training results using the last significant number of components. The left panel  
 1063 shows the previous version (fxTWA-PLS1) and the right panel shows the modified version of  
 1064 fxTWA-PLS (fxTWA-PLS2). The 1: 1 line is shown in black; the linear regression line is  
 1065 shown in red, to show the degree of overall compression. The horizontal dashed lines indicate  
 1066 the natural limit of  $\alpha$  (0~1.26).  
 1067



1068  
 1069

1070 Figure A2. Residuals using the last significant number of components. The left panel shows  
 1071 the previous version (fxTWA-PLS1) and the right panel shows the modified version (fxTWA-  
 1072 PLS2) of fxTWA-PLS. The zero line is shown in black; the locally estimated scatterplot  
 1073 smoothing is shown in red, to show the degree of local compression.  
 1074



1075

1076